

1.2.2 Reference Frames and Coordinate Systems

Reference frames as in Definition 1.1 allow defying the position and the motion of a vehicle independently from a reference observer's point of view. By selecting a coordinate system to which refer all the physical measures, the previous invariant tensor expressions can be numerically evaluated, thus enabling the implementation of software simulations. The most relevant reference frames and associated coordinate systems are presented hereafter.

Earth Frame (E). In classical physics, the position and motion of any physical object imply the designation of a common inertial reference frame. Depending on the specific application, three different inertial frames are commonly considered in the aerospace framework: Heliocentric frame (for planetary space travel), Geocentric-inertial and Earth frames (for Earth-orbiting satellites). The base points of the Geocentric-inertial and Earth frames are both located at the center of the Earth (E). However, the Geocentric-inertial frame assumes the Earth to have a fixed orientation on the ecliptic plane, while the Earth frame's base vectors (\mathbf{e}_1 , \mathbf{e}_2 , \mathbf{e}_3) follow the characteristic motion of rotation. As shown in Figure 1.1(a), \mathbf{e}_1 is directed to the intersection between the Greenwich meridian and the equator, while \mathbf{e}_3 is aligned with the Earth's axis of rotation, pointing to the North Pole. Despite being subjected to accelerations, the Earth frame is generally assumed inertial for any lower atmosphere flights, in reason of the negligible effect generated by the rotation (Assumption 1.1).

Body Frame (B). Under the Rigid Body Assumption 1.4, the investigated flying vehicle is commonly designated as a reference frame itself. This allows expressing its relative position and motion w.r.t. the selected inertial frame. In the body frame, the base point (B) corresponds to the vehicle's center of mass (CM), whereas the base vectors (\mathbf{b}_1 , \mathbf{b}_2 , \mathbf{b}_3) are aligned with the principal axes of the vehicle's inertia tensor, as shown in Figure 1.1(b): \mathbf{b}_1 generally points towards the nose of the vehicle along its longitudinal axis (rotational symmetry), \mathbf{b}_2 is parallel to the second principal moment of inertia axis, while \mathbf{b}_3 is directed downwards.

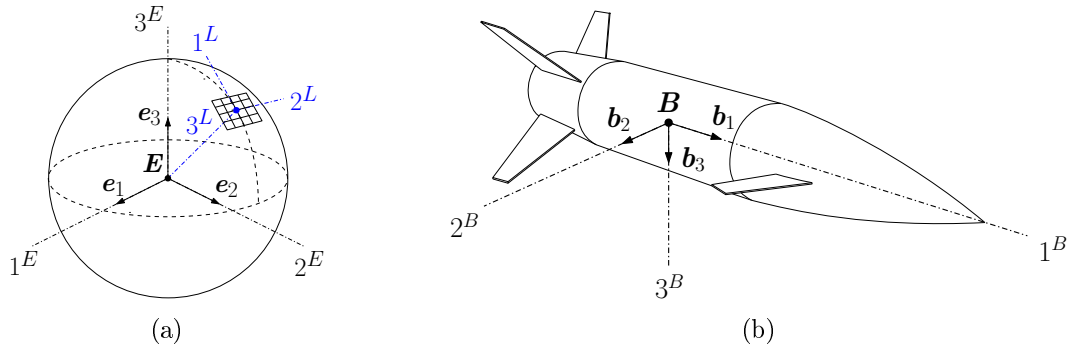


Figure 1.1: Main reference frames and coordinate systems: (a) Earth frame, E , and Earth and local-level coordinates; (b) body frame, B , and body coordinates.

Air Frame (A). Assuming the air mass to behave as a compact body¹, the air itself can be considered as a physical frame. The main base vector, \mathbf{a}_1 , follows the direction of the relative wind vector, \mathbf{v}_B^A , which describes the relative motion of the vehicle's CM w.r.t. the air frame. As later discussed, the air mass can be considered in motion w.r.t. the Earth frame or assumed at rest, $\mathbf{v}_E^A = 0$ (Zero Wind Assumption 1.3).

As previously mentioned, for atmospheric Earth-orbiting flying vehicles below the supersonic regime, the effects of the Earth's accelerations can be neglected, thus assuming the Earth as the inertial reference frame. As a consequence, the coordinate system associated with the Heliocentric frame as well as the related coordinate transformations are not considered for the purpose of this work.

Earth and Geographic Coordinate System. The preferred coordinate system associated with the Earth's frame has the three axes ($1^E, 2^E, 3^E$) aligned with the base vectors ($\mathbf{e}_1, \mathbf{e}_2, \mathbf{e}_3$), respectively, as shown in Figure 1.1(a). By subdividing the Earth's surface on a grid of vertical lines connecting the Poles (meridians) and lines parallel to the equator and concentric to the Poles (parallels), any location can be uniquely identified through the definition of its longitude, l , and latitude, λ , measures. The longitude is expressed as the angle (± 180 deg) from the Greenwich meridian in an easterly direction, while the latitude is the angle from the equator to the north (90 deg) or to the south (-90 deg). The geographic coordinate system, $]^G$, is associated with any specific pair (l, λ) and consists of an axis pointing to the north (1^G), an axis pointing to the center of the Earth (3^G), and a third axis which points east (2^G).

Local-level Coordinate System. The notion of geographic coordinates can be further generalized whenever the exact location (l, λ) of the vehicle on the Earth's surface does not relevantly affect the trajectory evaluation. This simplification implies the Flat Earth Assumption 1.2 since a geographic location is characterized by a specific surface curvature. Under this condition, any local plane tangent to the Earth's surface can be employed as a geographic coordinate system and is referred to as a local-level coordinate system, $]^L$. This system is generally associated with the launch point of the vehicle to properly express the vehicle's trajectory. Following the standard north-east-down (NED) convention, axes 1^L and 2^L lie in the tangent plane, respectively pointing north and east, while axis 3^L points downward to the center of the Earth, as shown in Figure 1.1(a).

Body Coordinate System. The body coordinate system, $]^B$, corresponds to the preferred system associated with the body frame, having the axes ($1^B, 2^B, 3^B$) respectively aligned with the base vectors ($\mathbf{b}_1, \mathbf{b}_2, \mathbf{b}_3$). The relative transformation between the body and the local-level coordinates allows defining the orientation of the vehicle across the trajectory through the Euler angles (ϕ, θ, ψ). The overall coordinate transformation is obtained through a sequential set of rotations complying with the standard aircraft intermediate coordinate systems, $]^X$ and $]^Y$. A first yaw angle rotation, ψ , about the vertical axis (3^L) defines the intermediate system

¹No relative motion among the air particles.

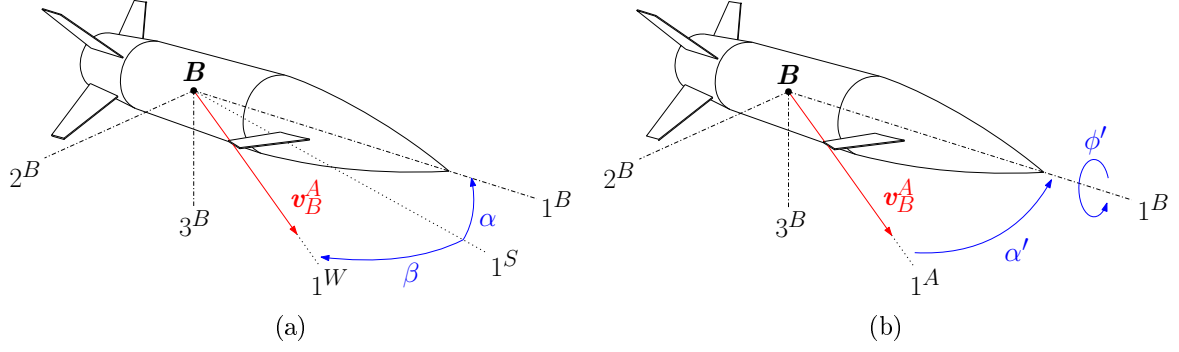


Figure 1.2: Wind coordinate systems: (a) Cartesian incidence angles convention; (b) polar aeroballistic angles convention.

$]^X$, while a second pitch angle rotation, θ , about the lateral axis (2^X) leads to the intermediate system, $]^Y$. The final roll rotation, ϕ , about the longitudinal axis (1^Y) completes the sequence.

$$[\mathbf{T}]^{BY} = \begin{bmatrix} 1 & 0 & 0 \\ 0 & \cos \phi & \sin \phi \\ 0 & -\sin \phi & \cos \phi \end{bmatrix}; \quad [\mathbf{T}]^{YX} = \begin{bmatrix} \cos \theta & 0 & -\sin \theta \\ 0 & 1 & 0 \\ \sin \theta & 0 & \cos \theta \end{bmatrix}; \quad [\mathbf{T}]^{XL} = \begin{bmatrix} \cos \psi & \sin \psi & 0 \\ -\sin \psi & \cos \psi & 0 \\ 0 & 0 & 1 \end{bmatrix}.$$

By multiplying the set of sequential transformations in the proper order, the complete body to local-level coordinate transformation is expressed as:

$$\begin{aligned} [\mathbf{T}]^{BL} &= [\mathbf{T}]^{BY} [\mathbf{T}]^{YX} [\mathbf{T}]^{XL} \\ &= \begin{bmatrix} \cos \psi \cos \theta & \sin \psi \cos \theta & -\sin \theta \\ \cos \psi \sin \theta \sin \phi - \sin \psi \cos \phi & \sin \psi \sin \theta \sin \phi + \cos \psi \cos \phi & \cos \theta \sin \phi \\ \cos \psi \sin \theta \cos \phi + \sin \psi \sin \phi & \sin \psi \sin \theta \cos \phi - \cos \psi \sin \phi & \cos \theta \cos \phi \end{bmatrix}. \end{aligned}$$

Wind Coordinate System. The last relevant coordinate system to be defined is associated with the air frame. The axis 1^W is aligned with the relative velocity direction v_B^A , while the other two axes are defined based on the selected convention:

❖ **Cartesian Incidence Angles.** The body to wind coordinate transformation of any vehicle characterized by a planar symmetry relies on the definition of an intermediate stability coordinate system, $]^S$, as shown in Figure 1.2(a). The first axis, 1^S , corresponds to the projection of v_B^A in the plane ($1^B, 3^B$), identifying the angle-of-attack (AoA), α , as the positive rotation angle from 1^S to 1^B . Similarly, the lateral angle-of-sideslip (AoS), β , is defined as the positive rotation angle from 1^S to 1^W . The body to wind transformation matrix is expressed as follows:

$$[\mathbf{T}]^{WB} = \begin{bmatrix} \cos \alpha \cos \beta & \sin \beta & \sin \alpha \cos \beta \\ -\cos \alpha \sin \beta & \cos \beta & -\sin \alpha \sin \beta \\ -\sin \alpha & 0 & \cos \alpha \end{bmatrix}. \quad (1.7)$$

❖ **Polar Aeroballistic Angles.** Concerning rotational symmetric vehicles, a different intermediate aeroballistic coordinate system, \mathcal{J}^R , is defined. This coordinate system is aligned with the load factor plane of the vehicle, where the main aerodynamic interactions are generated (Drag and Lift forces). The axis 1^R coincides with 1^B and lies in the load factor plane together with 3^R . A first aerodynamic roll angle rotation, ϕ' , about the axis 1^R defines the aeroballistic to body coordinate transformation. The final aeroballistic wind coordinate system, \mathcal{J}^A , is reached through the total angle-of-attack rotation, α' , about the 2^A axis, defined positive from 1^B to 1^A (equal to 1^W and aligned with \mathbf{v}_B^A). The axis 3^A lies in the load factor plane, as shown in Figure 1.2(b).

$$[\mathbf{T}]^{AB} = \begin{bmatrix} \cos \alpha' & \sin \alpha' \sin \phi' & \sin \alpha \cos \beta \\ -\cos \alpha \sin \beta & \cos \beta & -\sin \alpha \sin \beta \\ -\sin \alpha & 0 & \cos \alpha \end{bmatrix}. \quad (1.8)$$

1.2.3 6-DoF Projectile Equations of Motion

The formulation of the projectile nonlinear dynamics relies on the standard flight mechanics theory, complying with the notation proposed in [Zip14]; [Zip19]. The equations of motion describing the translational and attitude dynamics are first derived in an invariant tensor form and then projected w.r.t. the most appropriate system of coordinates, allowing for numerical computation. The derivation is based on the following modeling assumptions:

Assumption 1.1

The Earth is assumed as the inertial reference frame (E) since the centrifugal and Coriolis accelerations are negligible when dealing with subsonic atmospheric vehicle's trajectories.

Assumption 1.2 (Flat Earth)

The Earth's surface is assumed flat, neglecting the local eccentricity of the specific geographic location where the trajectory occurs.

Assumption 1.3 (Zero Wind)

The air mass is assumed at rest (no relative motion between frames A and E , $\mathbf{v}_E^A = 0$).

Assumption 1.4 (Rigid Body)

The projectile is considered a rigid body with constant and uniform mass distribution.

The translational and attitude dynamics express the relative linear and angular motions between frames B and E . The equations are derived from Newton's and Euler's laws, assuming the aerodynamic forces, \mathbf{f}_a , and the gravitational acceleration, \mathbf{g} , to be the only external effects contributing to the projectile dynamics. In particular, the gravity acceleration is applied on the projectile's center of mass (CM), while the aerodynamic forces are applied on the center

of pressure (CP), generating relevant moment contributions, \mathbf{m}_B , w.r.t. the CM:

$$\begin{aligned} m\mathcal{D}^E \mathbf{v}_B^E &= \mathbf{f}_a + m\mathbf{g}, \\ \mathcal{D}^E \mathbf{l}_B^{BE} &= \mathbf{m}_B. \end{aligned} \quad (1.9)$$

where m is the constant mass of the projectile, \mathbf{v}_B^E represents the relative velocity of the CM w.r.t. the Earth reference frame, and \mathbf{l}_B^{BE} is the angular momentum between the body and the Earth frames, expressed again w.r.t. the CM.

Since the translational and attitude dynamics have to be expressed in the body coordinates, the rotational time derivative operator w.r.t. the Earth frame, \mathcal{D}^E , is shifted to the body frame through the Euler transformation discussed in Theorem 1.1. By expanding $\mathbf{l}_B^{BE} = \mathbf{I}_B^B \boldsymbol{\omega}^{BE}$, where \mathbf{I}_B^B is the moment of inertia (MoI) of the body referred to the CM, and $\boldsymbol{\omega}^{BE}$ represents the relative angular velocity between the body and the Earth frames, the tensor Equation (1.9) become:

$$\begin{aligned} m\mathcal{D}^B \mathbf{v}_B^E + m\boldsymbol{\Omega}^{BE} \mathbf{v}_B^E &= \mathbf{f}_a + m\mathbf{g}, \\ \mathbf{I}_B^B \mathcal{D}^B \boldsymbol{\omega}^{BE} + \boldsymbol{\Omega}^{BE} \mathbf{I}_B^B \boldsymbol{\omega}^{BE} &= \mathbf{m}_B. \end{aligned} \quad (1.10)$$

In order to enable numerical calculations, Equation (1.10) is projected in the body coordinates. The gravity contribution, simplified to a constant quantity pointing to the center of the Earth, is more appropriately expressed in the local-level coordinates as $[\mathbf{g}]^L = [0 \ 0 \ g]^T$ and then coherently transformed to the body coordinate system:

$$\begin{aligned} m \left[\frac{d\mathbf{v}_B^E}{dt} \right]^B + m [\boldsymbol{\Omega}^{BE}]^B [\mathbf{v}_B^E]^B &= m [\mathbf{T}]^{BL} [\mathbf{g}]^L + [\mathbf{f}_a]^B, \\ [\mathbf{I}]_B^B \left[\frac{d\boldsymbol{\omega}^{BE}}{dt} \right]^B + [\boldsymbol{\Omega}^{BE}]^B [\mathbf{I}]_B^B [\boldsymbol{\omega}^{BE}]^B &= [\mathbf{m}_B]^B. \end{aligned}$$

The resulting set of state variables for the translational dynamics consists of the projectile's linear velocity projections along the body coordinate (u, v, w), while the attitude dynamics is expressed in terms of the projectile's body rates, namely the roll rate, p , the pitch rate, q , and the yaw rate, r , as shown in Figure 1.3:

$$[\mathbf{v}_B^E]^B = \begin{bmatrix} u \\ v \\ w \end{bmatrix}; \quad [\boldsymbol{\omega}^{BE}]^B = \begin{bmatrix} p \\ q \\ r \end{bmatrix}.$$

Moreover, the skew-symmetric form of the angular velocity tensor, $\boldsymbol{\omega}^{BE}$, and the MoI, are expressed respectively as:

$$[\boldsymbol{\Omega}^{BE}]^B = \begin{bmatrix} 0 & -r & q \\ r & 0 & -p \\ -q & p & 0 \end{bmatrix}; \quad [\mathbf{I}_B^B]^B = \begin{bmatrix} I_1 & 0 & 0 \\ 0 & I_2 & 0 \\ 0 & 0 & I_3 \end{bmatrix}. \quad (1.11)$$

In particular, the content of the MoI depends on the characteristic symmetry of the investigated vehicle. Rotational symmetric bodies like projectiles are generally characterized by a diagonal MoI since the product of inertia (I_{12} , I_{13} , I_{23}) are negligible ([Zip76]).

The translational dynamics can be finally expressed explicitly in the body coordinates as:

$$\begin{aligned}\frac{du}{dt} &= rv - qw + \frac{f_{a1}}{m} - g \sin \theta, \\ \frac{dv}{dt} &= pw - ru + \frac{f_{a2}}{m} + g \cos \theta \sin \phi, \\ \frac{dw}{dt} &= qu - pv + \frac{f_{a3}}{m} + g \cos \theta \cos \phi,\end{aligned}\tag{1.12}$$

while the attitude dynamics takes the form:

$$\begin{aligned}\frac{dp}{dt} &= I_1^{-1} [(I_2 - I_3) qr + m_{B1}], \\ \frac{dq}{dt} &= I_2^{-1} [(I_3 - I_1) pr + m_{B2}], \\ \frac{dr}{dt} &= I_3^{-1} [(I_1 - I_2) pq + m_{B3}].\end{aligned}\tag{1.13}$$

The expressions of the aerodynamic forces (f_{a_i}), and moments (m_{B_i}), with $i = 1, 2, 3$, are coherently projected in the body coordinates. The complete characterization of the projectile's aerodynamic model is detailed later in Section 1.3.

Concerning the kinematics computation, the projectile's position, \mathbf{s}_{BE} , is expressed w.r.t. the local-level coordinates (NED). The linear velocity, \mathbf{v}_B^E , obtained through the translational dynamics in Equation (1.12) in the body coordinates, is first converted to the local coordinates:

$$[\mathbf{v}_B^E]^L = [\mathbf{T}]^{BL,T} [\mathbf{v}_B^E]^B = \begin{bmatrix} u_L \\ v_L \\ w_L \end{bmatrix}\tag{1.14}$$

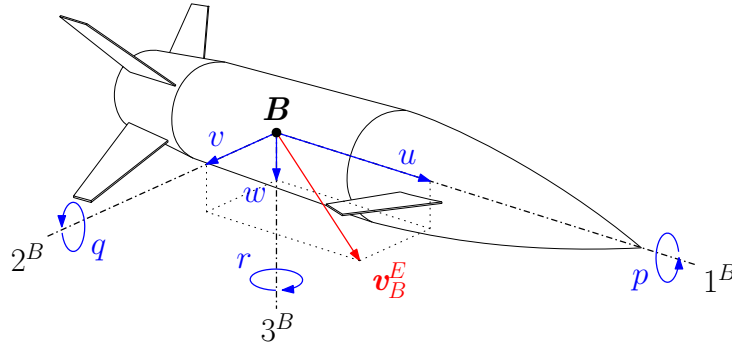


Figure 1.3: Projectile's linear and angular velocities components projected w.r.t. the body coordinates.

and then, the projectile's local position can be obtained through time integration:

$$\left[\frac{d\mathbf{s}_{BE}}{dt} \right]^L = [\mathbf{v}_B^E]^L. \quad (1.15)$$

In order to determine the projectile's orientation, the rotation tensor approach is preferred². It is based on the formulation of the rotational time derivative of the Direction Cosine Matrix (DCM), $[\mathbf{T}]^{BL}$ as:

$$\left[\frac{d\mathbf{T}}{dt} \right]^{BL} = [\boldsymbol{\Omega}^{BE}]^{B,T} [\mathbf{T}]^{BL}. \quad (1.16)$$

The resolution of the set of differential Equation (1.16) leads to the evaluation of the Euler angles (ϕ, θ, ψ) , as it follows:

$$\begin{aligned} \phi &= \arccos \left(\frac{\cos \theta \cos \phi}{\cos \theta} \right) \text{sign}(\cos \theta \sin \phi), \\ \theta &= \arcsin(\sin \theta), \\ \psi &= \arccos \left(\frac{\cos \psi \cos \theta}{\cos \theta} \right) \text{sign}(\sin \psi \cos \theta). \end{aligned} \quad (1.17)$$

The last fundamental relationship to be exploited associates the aerodynamic angles $(\alpha, \beta, \alpha', \phi')$ to the body linear velocities (u, v, w) . Indeed, the alternative formulation of the projectile's translational dynamics in terms of the aerodynamic angles is a common modeling approach for control-oriented design. Due to the Zero Wind Assumption 1.3, the simplification $\mathbf{v}_B^E = \mathbf{v}_B^A + \mathbf{v}_E^A = \mathbf{v}_B^A$ holds, thus the relative linear velocity of the body w.r.t. the air frame can be expressed in the body coordinates as $[\mathbf{v}_B^A]^B = [u \ v \ w]^T$. Since in the Cartesian wind coordinates the same linear velocity is projected as $[\mathbf{v}_B^A]^W = [V \ 0 \ 0]^T$, where V represents the airspeed, the following relation also holds:

$$\begin{bmatrix} V \\ 0 \\ 0 \end{bmatrix} = \begin{bmatrix} \cos \alpha \cos \beta & \sin \beta & \sin \alpha \cos \beta \\ -\cos \alpha \sin \beta & \cos \beta & -\sin \alpha \sin \beta \\ -\sin \alpha & 0 & \cos \alpha \end{bmatrix} \begin{bmatrix} u \\ v \\ w \end{bmatrix}; \quad \text{with } V = \sqrt{u^2 + v^2 + w^2}. \quad (1.18)$$

The expressions of the aerodynamic angles w.r.t the linear velocity projections in the body coordinates can be derived from Equation (1.18) as:

$$\alpha = \arctan \left(\frac{w}{u} \right); \quad \beta = \arcsin \left(\frac{v}{V} \right). \quad (1.19)$$

The same reasoning can be applied to evaluate the polar wind coordinates, leading to the following:

$$\alpha' = \arccos \left(\frac{u}{V} \right); \quad \phi' = \arctan \left(\frac{v}{w} \right).$$

²Singularities occur in the calculation when $\theta = \pm\pi/2$.

By inverting the relation, the linear velocities can be equivalently expressed w.r.t the aerodynamic angles as:

$$u = V \cos \alpha \cos \beta; \quad v = V \sin \beta; \quad w = V \sin \alpha \cos \beta. \quad (1.20)$$

The derivatives of Equations (1.18)-(1.19) allow defining the desired dynamics of the air variables:

$$\frac{dV}{dt} = \frac{u\dot{u} + v\dot{v} + w\dot{w}}{V}; \quad \frac{d\alpha}{dt} = \frac{u\dot{w} + w\dot{u}}{u^2 + w^2}; \quad \frac{d\beta}{dt} = \frac{-uv\dot{u} + (u^2 + w^2)\dot{v} - vw\dot{w}}{V^2\sqrt{u^2 + w^2}}.$$

Finally, by substituting Equation (1.12) and Equation (1.20) in the previous expressions, the translational dynamics formulated in the aerodynamic variables is obtained:

$$\begin{aligned} \frac{dV}{dt} &= \frac{1}{m} (f_{a1} \cos \alpha \cos \beta + f_{a2} \sin \beta + f_{a3} \sin \alpha \cos \beta) \\ &\quad + g (-\sin \theta \cos \alpha \cos \beta + \cos \theta \sin \phi \sin \beta + \cos \theta \cos \phi \sin \alpha \cos \beta), \\ \frac{d\alpha}{dt} &= \frac{1}{mV \cos \beta} (-f_{a1} \sin \alpha + f_{a3} \cos \alpha) + q \\ &\quad - (p \cos \alpha + r \sin \alpha) \tan \beta + \frac{g}{V \cos \beta} (\sin \theta \sin \alpha + \cos \theta \cos \phi \cos \alpha), \\ \frac{d\beta}{dt} &= \frac{1}{mV} (-f_{a1} \cos \alpha \sin \beta + f_{a2} \cos \beta - f_{a3} \sin \alpha \sin \beta) + p \sin \alpha - r \cos \alpha \\ &\quad + \frac{g}{V} (\sin \theta \cos \alpha \sin \beta + \cos \theta \sin \phi \cos \beta - \cos \theta \cos \phi \sin \alpha \sin \beta). \end{aligned} \quad (1.21)$$

1.2.4 The LRGP Concept

The model consists of a new concept of long range guided projectile (LRGP) investigated at the French-German Research Institute of Saint-Louis (ISL) ([Mar+18]; [Lib+19]; [Lib+20]; [Lib+21]). The interest motivating the project relies on the enhancement of the operating range capability of standard howitzer ammunition, avoiding the employment of any additional thruster propulsion or modifications of the firing system.

The projectile's design is based on a Secant Ogive Cylinder Boat Tail (SOCBT) geometry, with a full-scale 155 mm caliber and a non-rotating fin-stabilized architecture, including a set of four axial symmetrical tail-fins, and a reduced set of two front canards for control maneuvers ([Fre11]; [CFC12]). The employment of a non-spinning concept reduces the highly nonlinear dynamics generated by the aerodynamic coupling terms. Furthermore, the control canards are installed in a non-co-planar configuration ('X' configuration), as shown in Figure 1.4(a), aiming to reduce the overall canard-fin aerodynamic interaction, as well as the destabilizing effect generated by the canards aerodynamics.

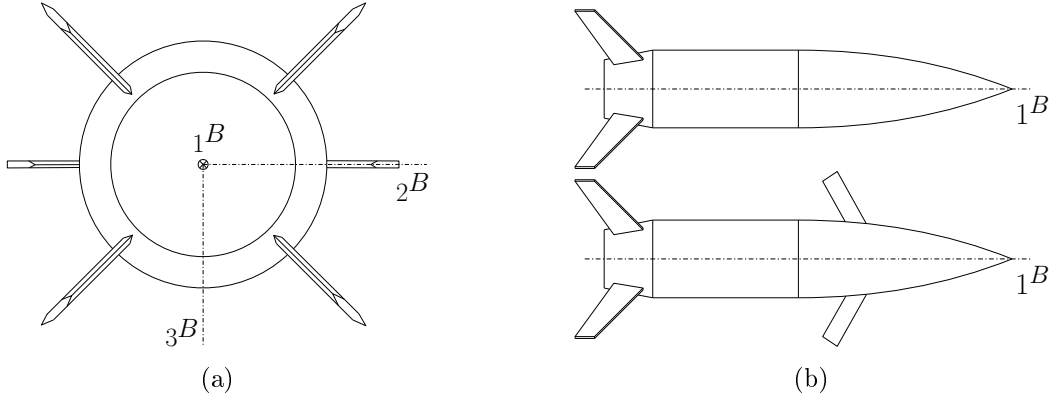


Figure 1.4: LRGP concept: (a) ‘X’ fins-canards configuration; (b) ballistic (top) and glider (bottom) projectile’s configuration.

The proposed flight strategy consists of an initial phase of ballistic trajectory, as in Figure 1.5, where the tail-fins are unfolded from the main sabot immediately after the firing occurs, while the canards remain folded to reduce the initial aerodynamic Drag. Once the apogee of the trajectory is reached, the canards are deployed, and the guided gliding phase begins. During this phase, the optimization of the projectile’s range performance relies on the engagement of an ad-hoc designed range-extension guidance law. Additionally, the employment of Bank-To-Turn (BTT) maneuvers is expected to smoothen the gliding trajectory, minimizing the lateral aerodynamic effects and optimizing the Lift contributions. In opposition to conventional Skid-To-Turn maneuvers, the BTT strategy aims to align the vertical plane of the projectile with the plane of maximum generated aerodynamic Lift through two consecutive maneuvers:

1. A banking motion about the airspeed vector that aligns the vertical plane to the plane of maximum aerodynamic Lift, minimizing the lateral displacement (ideally $\beta = 0$ deg).
2. An AoA correction to optimize the generated Lift-to-Drag Ratio (LDR).

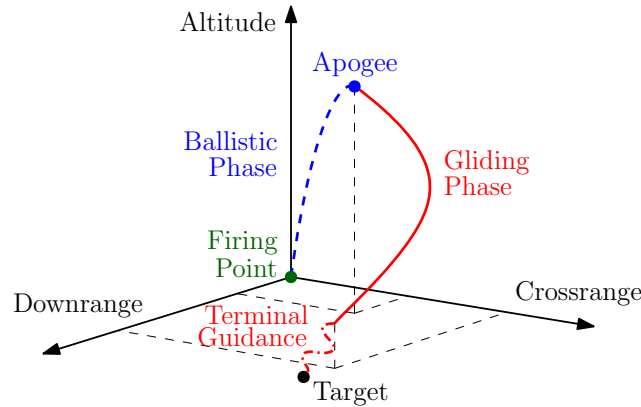


Figure 1.5: LRGP flight strategy: range-enhancement gliding trajectory.

By accounting for the specific configuration of the projectile and the flight strategy selected for the range improvement, the following assumptions can be defined to simplify the modeling and control design process:

Assumption 1.5 (Dynamic Decoupling)

The pitch and the roll-yaw channels of the projectile dynamics are assumed decoupled in reason of the limited lateral and roll effects generated by the BTT flight strategy.

Assumption 1.6 (Inertial Decoupling)

The non-co-planar configuration of the canards induces a slight geometrical asymmetry resulting in an overall second-order rotational symmetry. In this case, the inertia tensor expressed in Equation (1.11) is characterized by the relationship: $I_1 \ll I_2 < I_3$.

Based on the above considerations, for control-oriented modeling, the pitch and the roll-yaw channels can be designed separately ([Bla91]). During the control design stage, discussed in the next chapters, particular attention is dedicated to the pitch channel dynamics, being the main target of the range optimization process.

1.2.4.1 Pitch Channel Dynamics

The pitch channel dynamics is obtained by constraining the projectile's trajectory in the vertical (pitch) plane. In this context, the translational dynamics expressed w.r.t. the aerodynamic variables provides a more convenient model formulation in view of the control design. Thus, the AoA dynamics (short-period mode) in Equation (1.21) is coupled with the pitch rate dynamics (long-period mode) in Equation (1.13), neglecting the lateral contributions ($\beta \approx 0$ deg), and the roll-yaw coupling terms ($p, r \approx 0$ deg/s):

$$\begin{aligned} \frac{d\alpha}{dt} &= \frac{1}{mV} (-f_{a1} \sin \alpha + f_{a3} \cos \alpha) + q + \frac{g}{V} (\sin \theta \sin \alpha + \cos \theta \cos \phi \cos \alpha), \\ \frac{dq}{dt} &= \frac{m_{B2}}{I_2}. \end{aligned} \tag{1.22}$$

By including the airspeed dynamics, \dot{V} , in the model above, the complete formulation of the projectile longitudinal dynamics could be employed for the control design (also addressing the phugoid oscillation). However, the absence of any direct control authority on the longitudinal motion and the targeted control design approach makes this formulation unfeasible for the purposes of this study, as it will be explained in the next chapter. As a final remark, load factor measurements (LF), η_z , can be employed at the control design stage. They are generally modeled as:

$$\eta_z = \frac{f_{a3}}{mg}. \tag{1.23}$$

1.3 Projectile Aerodynamic Characterization

The complete derivation of the projectile flight dynamics implies an appropriate aerodynamic characterization. The mutual interaction between the projectile and the airflow is affected by several factors, such as the flow regime (Mach number, Reynolds number), the flight trajectory (incidence angles, body rates), the control actions (control surface deflections), and the projectile's geometry. The interaction generates a set of aerodynamic forces and corresponding moments (\mathbf{f}_a , \mathbf{m}_B), applied in the center of pressure (CP) of the body. Whenever a projectile is characterized by a CP located ahead of the CM, the contributions of the aerodynamic moments result in a destabilizing effect, deviating the system away from the desired trajectory. Nevertheless, unstable systems are also characterized by a more reactive aerodynamic response, providing generally higher maneuverability ([CFC12]). Thus, at the design stage, a compromise has to be reached between the required stability and performance properties.

1.3.1 Aerodynamics Formulation

The fundamental aerodynamic forces are generated in the load factor plane of any flying vehicle by the interaction with the airflow, in terms of Drag, D , and Lift, L , contributions ([McC99]). As shown in Equations (1.12)-(1.13), the aerodynamic forces and moments derived from the projections of Drag and Lift in the projectile's body coordinates are expressed as:

$$[\mathbf{f}_a]^B = \begin{bmatrix} f_{a1} \\ f_{a2} \\ f_{a3} \end{bmatrix} = \bar{q}S \begin{bmatrix} C_X \\ C_Y \\ C_Z \end{bmatrix}; \quad [\mathbf{m}_B]^B = \begin{bmatrix} m_{B1} \\ m_{B2} \\ m_{B3} \end{bmatrix} = \bar{q}Sd \begin{bmatrix} C_l \\ C_m \\ C_n \end{bmatrix}. \quad (1.24)$$

Specifically, S represents the body reference surface, d is the caliber, $\bar{q} = \frac{1}{2}\rho V^2$ is the dynamic pressure, and $\mathcal{M} = \frac{V}{a}$ is the Mach number. These quantities are defined as functions of the airspeed, V , and of the altitude-dependent air density, $\rho(h)$, and speed of sound, $a(h)$.

The projectile's aerodynamic characterization process relies on the derivation of the aerodynamic coefficients, C_i , with $i = X, Y, Z, l, m, n$. These non-dimensional coefficients are obtained either from real wind tunnel aerodynamic measurements, normalized by the vehicle's dimensions, or from sophisticated Computational Fluid Dynamic (CFD) software simulations. Due to the high technical costs implied by the development of real wind tunnel tests, CFD simulations are generally preferred for early modeling stages of the design optimization process, especially if several flight regimes are investigated (subsonic, and transonic flow). Each of the coefficients depends on a large number of flight parameters, as \mathcal{M} , the incidence angles, α and β (or α' and ϕ'), the body rates, p , q , and r , and the control deflections, accounted for in the measurements procedure.

Concerning the control deflections, the LRGP concept is equipped with two front canards (right and left), providing two independent local control deflections (δ_r , δ_l), as shown in Figure 1.6. However, for control-oriented modeling, the control actions are conventionally expressed in terms of roll, pitch, and yaw contributions (δ_p , δ_q , δ_r), respectively. This virtual set of control

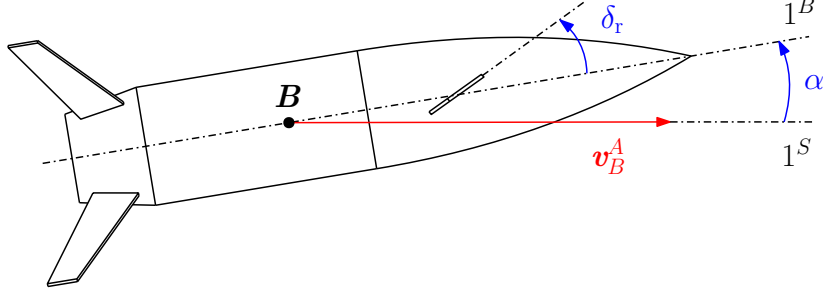


Figure 1.6: Canards local control deflection.

deflections is implemented through the selection of a dedicated control allocation logic. The availability of two horizontal front canards, aligned with the intent of improving the range capability of the projectile, suggested the employment of a BTT control strategy, leading to the definition of the static allocation matrix, \mathbf{T}_{CA} :

$$\begin{bmatrix} \delta_p \\ \delta_q \\ \delta_r \end{bmatrix} = \begin{bmatrix} -\frac{1}{2} & +\frac{1}{2} \\ +\frac{1}{2} & +\frac{1}{2} \\ 0 & 0 \end{bmatrix} \begin{bmatrix} \delta_r \\ \delta_l \end{bmatrix} = [\mathbf{T}_{CA}] \begin{bmatrix} \delta_r \\ \delta_l \end{bmatrix}. \quad (1.25)$$

1.3.2 Computational Fluid Dynamics Data

The design of the LRGP concept is based on a multi-objective aerodynamic optimization targeting both the range capability and the required time of flight to reach the target. The complete analysis is detailed in [BLM22]. The optimization aims to define fundamental geometrical features of the concept (fins and canards airfoil profile, canards sweep angle), having a relevant impact on the aerodynamic performance. Operational parameters such as the initial firing elevation angle of the gun, θ_e , the operating AoA range, and Mach regime are also considered. In reason of the extremely large computational complexity and the related processing time required to compute the aerodynamic optimization, a superposition hypothesis is proposed ([BLM22]).

Assumption 1.7 (Aerodynamic Superposition)

The aerodynamic control contributions, C_δ , provided by the local deflections of the control surfaces, δ , can be superposed to the general static effect, C_S , generated by the variation of the AoA on the overall projectile's body (including the control surfaces).

$$C = C_S \Big|_{\delta=0} (\alpha, \mathcal{M}) + C_\delta \Big|_{\alpha=0} (\delta, \mathcal{M}). \quad (1.26)$$

The aerodynamic coefficients are then parameterized through the superposition of several

mutually independent contributions as it follows:

$$\begin{aligned}
C_X(\mathcal{M}, \alpha, \beta, \delta_{\text{eff}}) &= C_{X_S}(\mathcal{M}, \alpha, \beta) + C_{X_{\delta_{\text{eff}}}}(\mathcal{M}, \delta_{\text{eff}}), \\
C_Y(\mathcal{M}, \alpha, \beta) &= C_{Y_S}(\mathcal{M}, \alpha, \beta) + \left(\frac{d}{2V}\right) C_{Y_r}(\mathcal{M}) r, \\
C_Z(\mathcal{M}, \alpha, \beta, \delta_q) &= C_{Z_S}(\mathcal{M}, \alpha, \beta) + \left(\frac{d}{2V}\right) C_{Z_q}(\mathcal{M}) q + C_{Z_{\delta_q}}(\mathcal{M}, \delta_q), \\
C_l(\mathcal{M}, \alpha, \beta, \delta_p) &= C_{l_S}(\mathcal{M}, \alpha, \beta) + \left(\frac{d}{2V}\right) C_{l_p}(\mathcal{M}) p + C_{l_{\delta_p}}(\mathcal{M}, \delta_p), \\
C_m(\mathcal{M}, \alpha, \beta, \delta_q) &= C_{m_S}(\mathcal{M}, \alpha, \beta) + \left(\frac{d}{2V}\right) C_{m_q}(\mathcal{M}) q + C_{m_{\delta_q}}(\mathcal{M}, \delta_q), \\
C_n(\mathcal{M}, \alpha, \beta) &= C_{n_S}(\mathcal{M}, \alpha, \beta) + \left(\frac{d}{2V}\right) C_{n_r}(\mathcal{M}) r,
\end{aligned} \tag{1.27}$$

where C_{i_S} represent the static aerodynamic contributions related to the projectile's body interaction with the airflow, C_{i_j} correspond to the dynamic damping effects, and $C_{i_{\delta_j}}$ are the additional aerodynamic contributions provided by the control surfaces deflections, with $i = X, Y, Z, l, m, n$ and $j = p, q, r$. In particular, the longitudinal control deflection is expressed as the combined nonlinear contributions of roll and pitch, $\delta_{\text{eff}} = \sqrt{\delta_p^2 + \delta_q^2}$.

As stated in Assumption 1.7, the superposition hypothesis relies on the idea that in the linear region of the canards' response (away from stall conditions), the aerodynamic contributions generated by the local control deflections (δ_r, δ_l) can be independently estimated and a posteriori added to the overall body contributions, which depend on the incidence angles ($\alpha', \phi', \alpha, \beta$). This allows for significantly reducing the computational complexity of the aerodynamic optimization by performing two independent campaigns of CFD simulations to characterize the projectile aerodynamics and define the geometrical properties of the concept.

1.3.2.1 Static Coefficients: ($C_{X_S}, C_{Y_S}, C_{Z_S}, C_{l_S}, C_{m_S}, C_{n_S}$)

The first CFD simulation campaign targets the static aerodynamic characterization of the full projectile's body by estimating the aerodynamic forces and moments coefficients: $C_{X_S}, C_{Y_S}, C_{Z_S}, C_{l_S}, C_{m_S}, C_{n_S}$. Two different datasets were acquired, one characterizing the ballistic configuration employed during the ascending phase of the trajectory, and one concerning the gliding configuration, including the static effect of the control surfaces at zero local deflections ($\delta_r, \delta_l = 0$ deg). Both the configurations are shown in Figure 1.4(b).

	\mathcal{M}	α' (deg)	ϕ' (deg)	δ_r, δ_l (deg)
min	0.3	0	0	0
max	1	16	90	0

Table 1.1: Static coefficients CFD acquisition ranges.

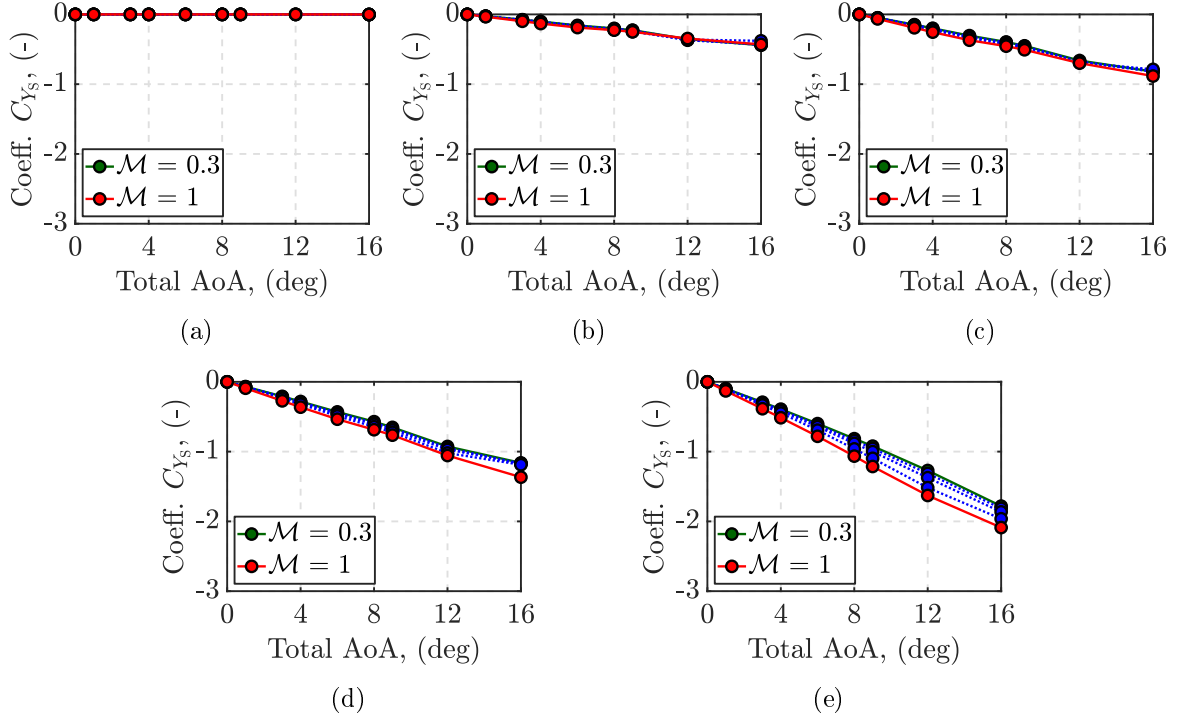


Figure 1.7: CFD static lateral coefficient dataset, C_{Y_s} : (a) $\phi' = 0$ deg; (b) $\phi' = 15$ deg; (c) $\phi' = 30$ deg; (d) $\phi' = 45$ deg; (e) $\phi' = 90$ deg.

The data were acquired as a function of \mathcal{M} in the subsonic/transonic regime, and of the polar angles α' and ϕ' , more suitable for the CFD software environment, assuming the variation ranges in Table 1.1.

Thus, for any pair (\mathcal{M}, ϕ') , the coefficients were investigated across the variation of α' . A sample of the acquisition results is presented in Figure 1.7, concerning the lateral coefficient C_{Y_s} in the gliding configuration.³ The complete dataset of aerodynamic measurements is provided in Appendix A.1. For modeling coherence, the coefficients have been converted a posteriori as a function of the Cartesian incidence angles (α, β) based on the transformations:

$$\alpha = \arctan(\tan \alpha' \cos \phi'); \quad \beta = \arcsin(\sin \alpha' \sin \phi'). \quad (1.28)$$

At higher values of ϕ' correspond an increasing dependence of the coefficients w.r.t. β and vice versa, defining the following limit aerodynamic configurations:

Conf₁: for $\phi' = 0^\circ \rightarrow \alpha' = \alpha$, the aerodynamic coefficients depend only on α .

Conf₂: for $\phi' = 90^\circ \rightarrow \alpha' = \beta$, the aerodynamic coefficients depend only on β .

³The coefficients' values have been normalized in reason of confidentiality.

1.3.2.2 Stability and Control Considerations

The aerodynamic stability of any vehicle is a fundamental aspect to be extensively investigated from the design stage. Indeed, a higher instability increases the complexity of the autopilot design. On the other hand, highly unstable vehicles are characterized by a responsive dynamics, capable to perform sharper and more aggressive maneuvers. Concerning the LRGP concept, an exhaustive aerodynamics analysis has been developed to find a proper compromise between stability and operating range performance.

The former property is generally analyzed through the variation of the relative position between the CP and the CM, $X_{CP,CM}$, or equivalently through the value of the pitching moment coefficient, C_{m_s} . Indeed, negative $X_{CP,CM}$ values correspond to the generation of a negative stabilizing C_{m_s} , which tends to maintain the direction of the projectile aligned with the relative velocity \mathbf{v}_B^A , minimizing the AoA. The canards installed in the front part of the projectile produce an aerodynamic Lift contribution that moves the overall CP of the projectile ahead. Thus, a design compromise has to be achieved between the improvement in the range performance and the unwanted destabilizing effect generated by the canards. The results presented in Figure 1.8 show the variation of the coefficient C_{m_s} as a function of the AoA and the Mach number.⁴ The LRGP concept is characterized by a predominantly unstable behavior, since the coefficient C_{m_s} is positive across most of the flight domain.

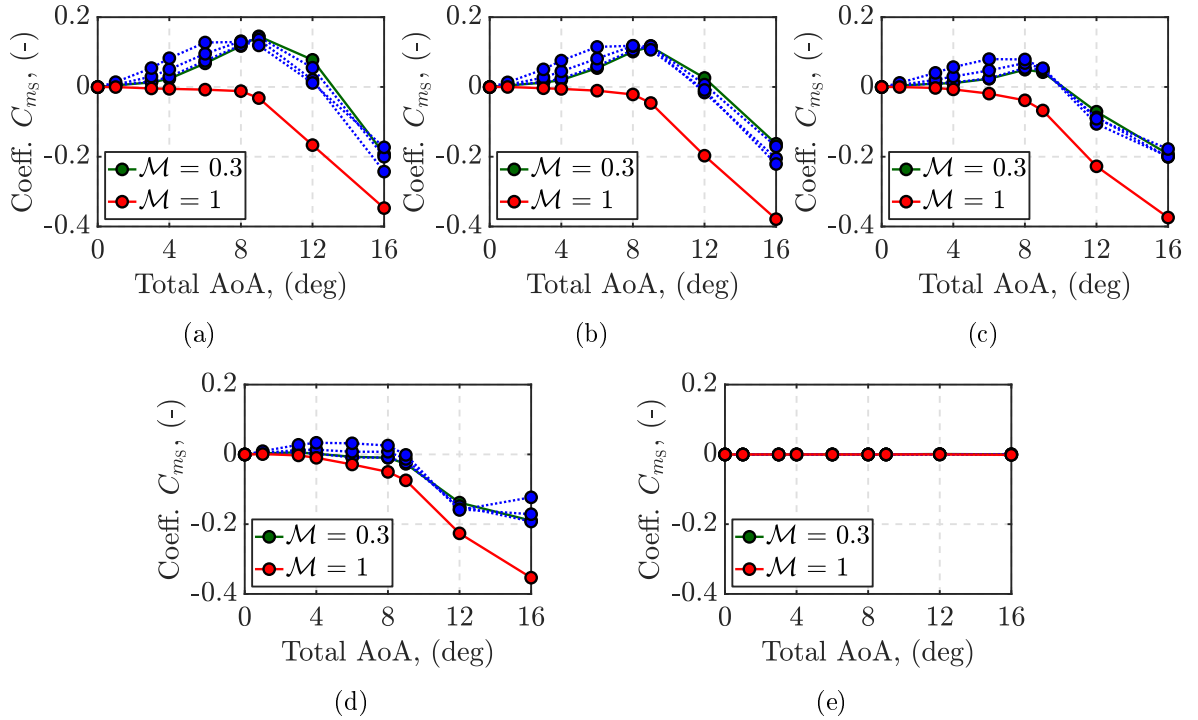


Figure 1.8: CFD static pitching moment coefficient dataset, C_{m_s} : (a) $\phi' = 0^\circ$; (b) $\phi' = 15^\circ$; (c) $\phi' = 30^\circ$; (d) $\phi' = 45^\circ$; (e) $\phi' = 90^\circ$.

⁴The coefficients' values have been normalized in reason of confidentiality.

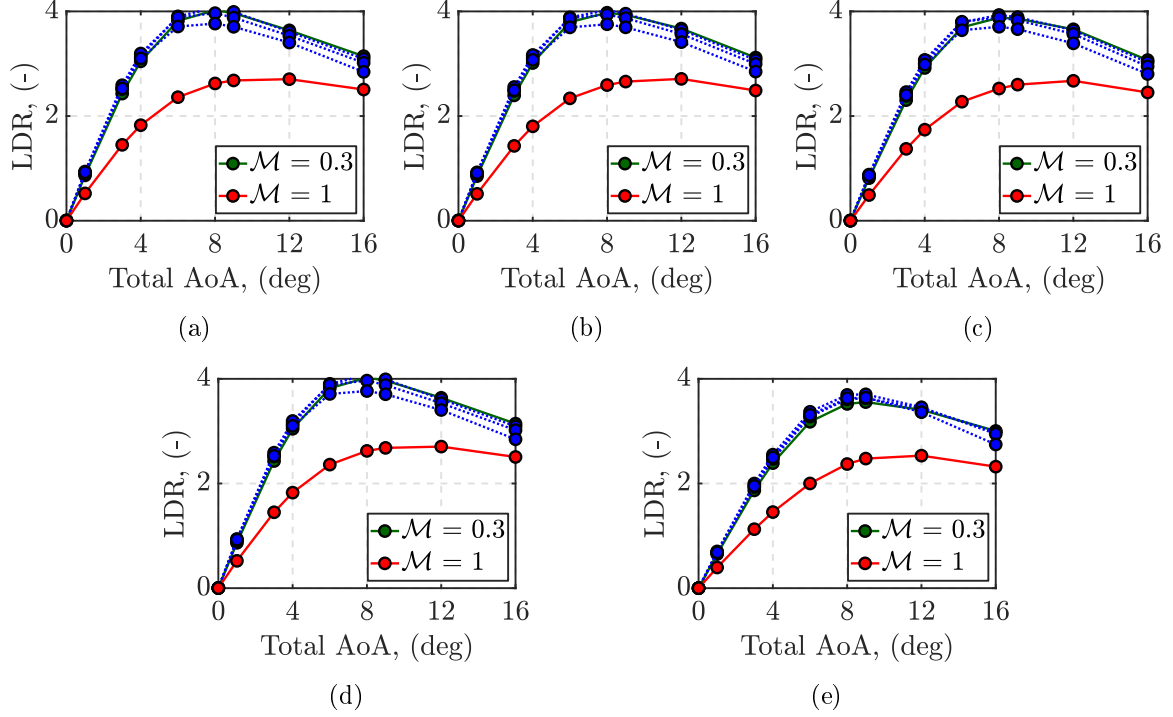


Figure 1.9: CFD Lift-to-Drag Ratio dataset, LDR: (a) $\phi' = 0$ deg; (b) $\phi' = 15$ deg; (c) $\phi' = 30$ deg; (d) $\phi' = 45$ deg; (e) $\phi' = 90$ deg.

The aerodynamic stability tends to improve at higher values of AoA (> 10 deg), and towards the transonic regime ($\mathcal{M} \approx 1$). Additionally, the pitching moment contribution decreases significantly as the aerodynamic roll angle increases. The range efficiency is estimated through the variation of the Lift-to-Drag Ratio index, $LDR = C_L/C_D$. At the concept design stage, this index suggests the optimal aerodynamic configuration to be selected in terms of canards/fins sweep angles, cant angles, and geometrical dimensions.

The variation of the LDR w.r.t. the aerodynamic variables, such as AoA, AoS, roll angle, and Mach, is also employed during the definition of the guidance law to find the flight conditions that optimize the projectile performance. The results of the analysis shown in Figure 1.9, reveal an optimal LDR index for a total AoA $\in [5, 10]$ deg, with a peak around 8 deg. The LDR decreases dramatically during the transition from subsonic to transonic regime, in reason of the lower Lift contribution generated by the turbulent airflow.

1.3.2.3 Control Coefficients ($C_{X_{\delta_{\text{eff}}}}$, $C_{Z_{\delta_q}}$, $C_{l_{\delta_p}}$, $C_{m_{\delta_q}}$)

The second CFD simulation campaign focused on the analysis of the aerodynamic control coefficients ($C_{X_{\delta_{\text{eff}}}}$, $C_{Z_{\delta_q}}$, $C_{l_{\delta_p}}$, $C_{m_{\delta_q}}$) generated by the canards' local deflections, δ_r and δ_l . The data were acquired only w.r.t. the local right canard deflection, δ_r , assuming the variation ranges in Table 1.2. The aerodynamic coefficients related to the left canard deflection, δ_l , can be easily obtained by means of symmetrical considerations.

	\mathcal{M}	α' (deg)	ϕ' (deg)	δ_r, δ_l (deg)
min	0.3	0	0	0
max	1	0	0	36

Table 1.2: Control coefficients CFD acquisition ranges.

During the acquisition, the angles ϕ' and α' were set to zero, and the residual static contributions generated by the projectile's body were subtracted in post-processing as:

$$\begin{pmatrix} C_{X_{\delta_r}} \\ C_{Z_{\delta_r}} \\ C_{l_{\delta_r}} \\ C_{m_{\delta_r}} \end{pmatrix} = \begin{pmatrix} C_{X_{\delta_r}} \\ C_{Z_{\delta_r}} \\ C_{l_{\delta_r}} \\ C_{m_{\delta_r}} \end{pmatrix} (\delta_r, \mathcal{M}) - \begin{pmatrix} C_{X_{\delta_r}} \\ C_{Z_{\delta_r}} \\ C_{l_{\delta_r}} \\ C_{m_{\delta_r}} \end{pmatrix} (\delta_r = 0, \mathcal{M}).$$

The results of the acquisitions for each control coefficient are presented in Figure 1.10.⁵ The specific canards configuration does not provide any control authority on the yaw plane, thus the lateral contributions $C_{Y_{\delta_r}}$ and $C_{n_{\delta_r}}$ are not considered. The modeling procedure employed to convert the measured coefficients, $(C_{X_{\delta_r}}, C_{Z_{\delta_r}}, C_{l_{\delta_r}}, C_{m_{\delta_r}})$, into the corresponding virtual counterparts, $(C_{X_{\delta_{\text{eff}}}}, C_{Z_{\delta_q}}, C_{l_{\delta_p}}, C_{m_{\delta_q}})$, is discussed in detail in Section 1.3.3.4.

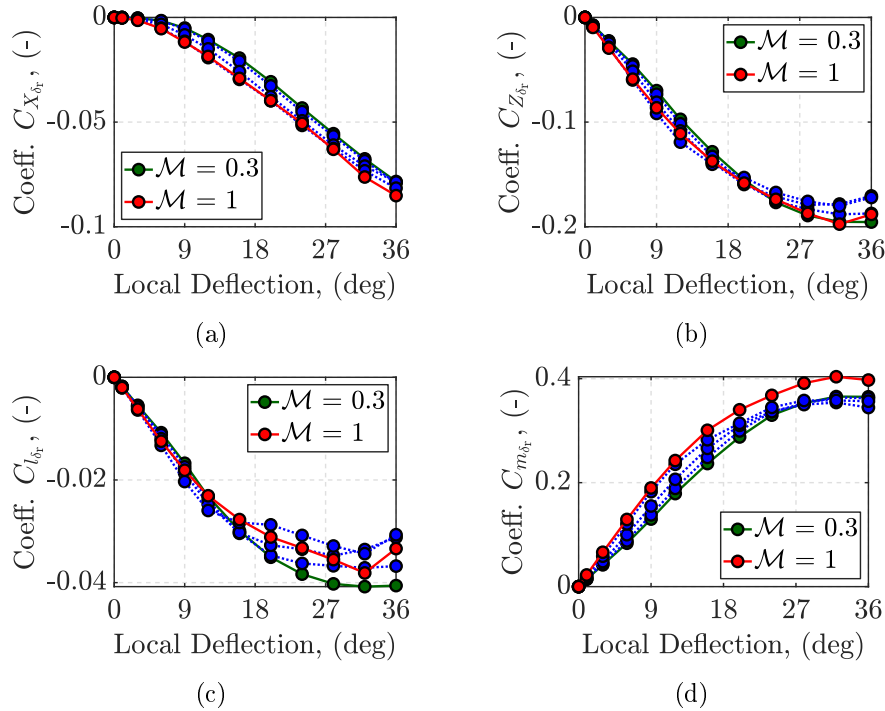


Figure 1.10: CFD control coefficient dataset: (a) longitudinal force, $C_{X_{\delta_r}}$; (b) vertical force, $C_{Z_{\delta_r}}$; (c) rolling moment, $C_{l_{\delta_r}}$; (d) pitching moment, $C_{m_{\delta_r}}$.

⁵The coefficients' values have been normalized to a range [0,1] in reason of confidentiality.

1.3.3 Aerodynamics Modeling

The results of the CFD acquisitions can be implemented in simulation either by direct interpolation of the obtained tables of measurements or through Taylor expansion by decomposing each coefficient in a set of derivative components ([Zip14]; [McC99]). The former approach is preferred during the initial ballistic ascending phase of the projectile's trajectory, while for control-oriented modeling, a continuous regression model is generally derived to characterize the aerodynamics of the guided phase.

In reason of the Aerodynamic Superposition Assumption 1.7, the static and control CFD datasets are analyzed separately:

- ❖ **Static:** two different regression models are proposed. A first model accounts only for the decoupled dynamics (pitch - roll/yaw), where the aerodynamics is either dependent on the variation of α (Conf₁) or β (Conf₂). This formulation is coherent with the dynamics developed for control design purposes in Equations (1.22)-(1.23). The second model accounts for the simultaneous variation of α and β induced by $\phi' \in (0, 90)$ deg. The regression is based on a multivariable approach and the resulting model is employed in the 6-DoF simulator environment to validate the controller design. The two regression analyses are discussed in Sections 1.3.3.1 and 1.3.3.2, respectively.
- ❖ **Control:** the CFD data acquired in terms of individual local canard variations (δ_r) are first modeled through a single variable regression analysis. Complying with the general aerodynamic parametrization in Equation (1.27), the resulting regression models are reformulated w.r.t. the virtual deflections set (δ_{eff} , δ_p , δ_q). The overall control modeling procedure is presented in Section 1.3.3.4.

1.3.3.1 Polynomial Regression (Static) Model

The first regression analysis relies on a reduced set of the static aerodynamic CFD coefficients, corresponding to the data related to the extreme configurations: Conf₁ and Conf₂. In the former scenario, the aerodynamic coefficients are measured across the variation of α , ideally without any contribution deriving from β . The latter configuration addresses the opposite scenario, since the aerodynamics of the projectile strictly depends on the variation of β . The dependence of the coefficients on the \mathcal{M} variation is not explicitly modeled by the regression analysis. Thus, the regression is performed for all the considered Mach conditions, and the results are tabulated for directed online interpolation during the simulations.

These assumptions allow the employment of a polynomial regression approach based on least-squares optimization ([Ost12]). Several polynomial models of increasing order have been investigated for each of the aerodynamic coefficients, aiming to find the best compromise between regression accuracy and model complexity. In particular, for the pitch plane coefficients (C_{Z_s} , C_{m_s}), only the α dependence is investigated in reason of the dynamics decoupling. Similarly, for the yaw plane coefficients (C_{Y_s} , C_{n_s}), only the β dependence is considered. The only

exceptions occur for the longitudinal coefficient, C_{X_S} , since the variations of α and β generate the same contribution due to the projectile's axial symmetry, and for the roll coefficient, C_{l_S} , which is negligible in reason of the fin-stabilized configuration of the projectile. The regression models are parameterized as follows:

$$\begin{aligned}
C_{X_S}(\mathcal{M}, \alpha) &= C_{X_{\alpha 0}}(\mathcal{M}) + \sum_{i=2}^N C_{X_{\alpha i}}(\mathcal{M}) \sin^i \alpha, \\
C_{Y_S}(\mathcal{M}, \beta) &= \sum_{j=1}^M C_{Y_{\beta j}}(\mathcal{M}) \sin^j \beta, \\
C_{Z_S}(\mathcal{M}, \alpha) &= \sum_{j=1}^M C_{Z_{\alpha j}}(\mathcal{M}) \sin^j \alpha, \\
C_{m_S}(\mathcal{M}, \alpha) &= \sum_{j=1}^M C_{m_{\alpha j}}(\mathcal{M}) \sin^j \alpha, \\
C_{n_S}(\mathcal{M}, \beta) &= \sum_{j=1}^M C_{n_{\beta j}}(\mathcal{M}) \sin^j \beta.
\end{aligned} \tag{1.29}$$

where $i = 2, 4, \dots, N$ is an even polynomial order sequence, while $j = 1, 3, \dots, M$ is an odd polynomial order sequence.

The accuracy of the data regressions is assessed at each \mathcal{M} condition by evaluating the statistical indexes: Root Mean Square Error (RMSE) and Coefficient of Determination (R^2). In particular, the RMSE values have been normalized by the difference between the maximum and the minimum values of the CFD data (Min-Max), providing an estimation of the relative regression error (NRMSE). The R^2 and NRMSE results obtained during the regression of the relevant α coefficient derivatives are displayed in Figure 1.11, while the β coefficient derivatives are presented in Figure 1.12. The model selection criteria consist of a correlation index $R^2 > 0.9$ and a relative regression error $\text{NRMSE} < 10\%$.

Based on the statistical results, the following *Polynomial Regression* (PR) aerodynamic model was selected as a compromise between accuracy and model complexity:

$$\begin{aligned}
C_{X_S}(\mathcal{M}, \alpha) &= C_{X_{\alpha 0}}(\mathcal{M}) + C_{X_{\alpha 2}}(\mathcal{M}) \sin^2 \alpha + C_{X_{\alpha 4}}(\mathcal{M}) \sin^4 \alpha, \\
C_{Y_S}(\mathcal{M}, \beta) &= C_{Y_{\beta 1}}(\mathcal{M}) \sin \beta, \\
C_{Z_S}(\mathcal{M}, \alpha) &= C_{Z_{\alpha 1}}(\mathcal{M}) \sin \alpha, \\
C_{m_S}(\mathcal{M}, \alpha) &= C_{m_{\alpha 1}}(\mathcal{M}) \sin \alpha + C_{m_{\alpha 3}}(\mathcal{M}) \sin^3 \alpha + C_{m_{\alpha 5}}(\mathcal{M}) \sin^5 \alpha, \\
C_{n_S}(\mathcal{M}, \beta) &= C_{n_{\beta 1}}(\mathcal{M}) \sin \beta.
\end{aligned} \tag{1.30}$$

The main justification behind the choice of sinusoidal regression polynomials relies on the complexity of modeling the projectile aerodynamics across the transonic regime ($\mathcal{M} > 0.7$), characterized by a highly nonlinear variation.

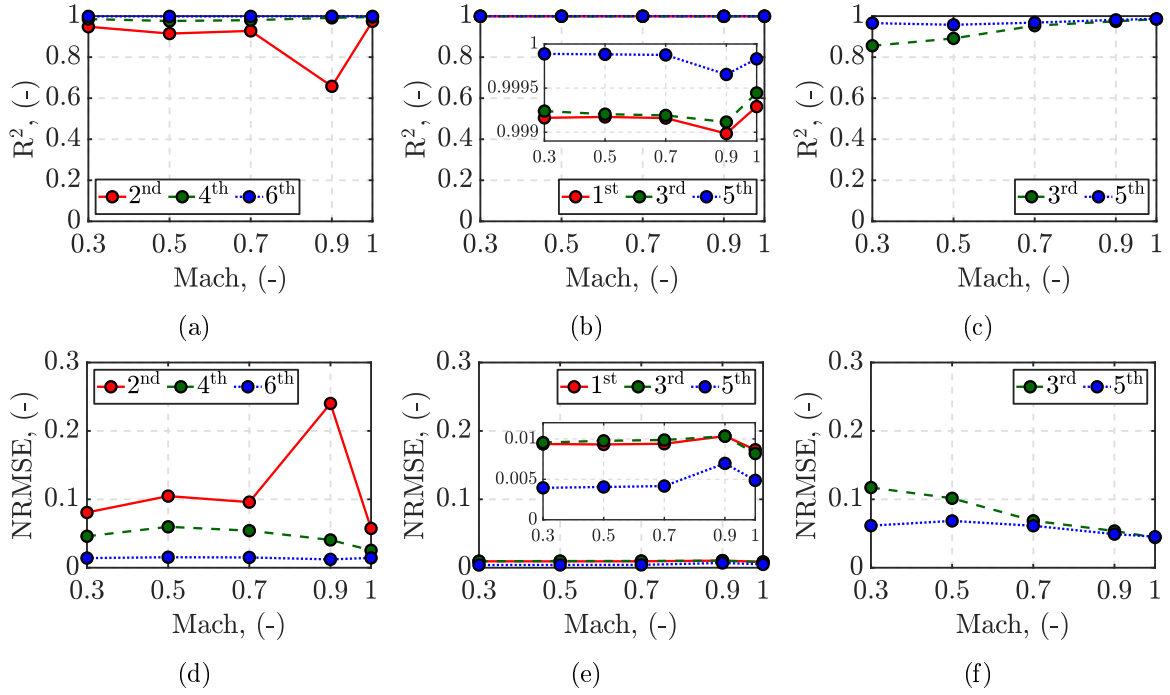


Figure 1.11: R^2 and NRMSE regression results: (a)-(d) longitudinal force coefficient, C_{X_S} ; (b)-(e) vertical force coefficient, C_{Z_S} ; (c)-(f) pitching moment coefficient, C_{m_S} .

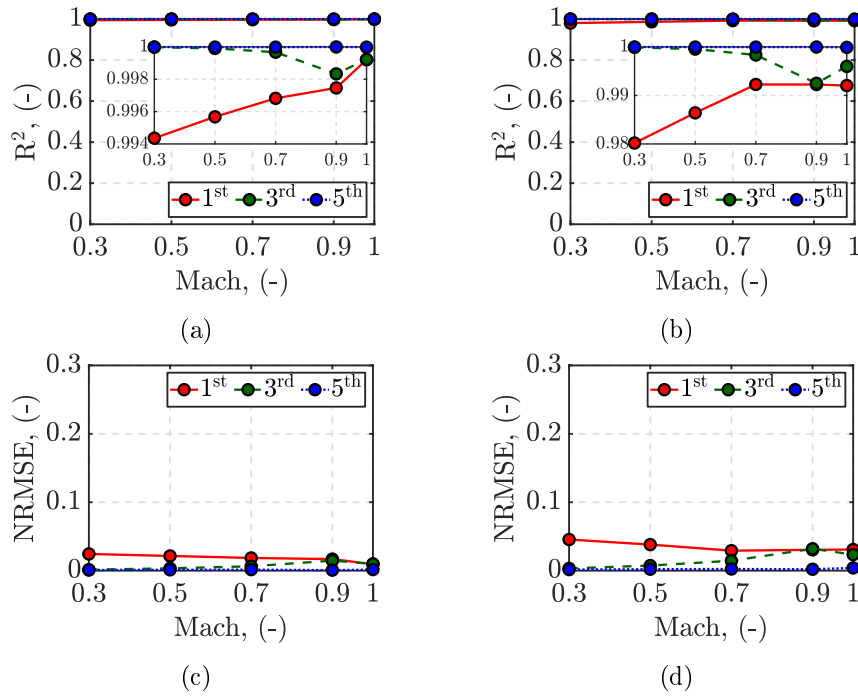


Figure 1.12: R^2 and NRMSE regression results: (a)-(c) lateral force coefficient, C_{Y_S} ; (b)-(d) yawing moment coefficient, C_{n_S} .

1.3.3.2 Multivariable Regression (Static) Model

The second regression analysis relies on the entire available CFD static aerodynamic dataset, also addressing the coupling effects generated by the simultaneous variation of the incidence angles, α and β (equivalently, $\phi' \in [0, 90]$ deg). Since the analysis involves several variables, different sets of multivariable models have been selected for the data regression. As assumed in the previous analysis, the dependence on \mathcal{M} is not exploited in the model to avoid an excessively complicated formulation. Each of the coefficients has been investigated considering several models. However, only the most relevant ones are discussed hereafter.

Model₁: this model is obtained from the theoretical flight mechanics and aerodynamics formulation proposed in [McC99]. The aerodynamic forces and moments are expressed in the tensor form in terms of Drag and Lift contributions, generated in the projectile's load factor plane, and then projected in the aeroballistic wind coordinate system. By employing the coordinate transformation in Equation (1.7), the resulting forces and moments are expressed w.r.t. the body coordinates as a function of the Cartesian incidence angles (α, β). These final Cartesian projections are employed as regression models. The full derivation of these models is detailed in Appendix A.2. As a result, the first multivariable regression model corresponds to the following:

$$\begin{aligned}
 C_{X_S}(\mathcal{M}, \alpha, \beta) &= C_{X_0}(\mathcal{M}) + C_{X_2}(\mathcal{M}) \cos \alpha \cos \beta + C_{X_4}(\mathcal{M}) \cos^2 \alpha \cos^2 \beta, \\
 C_{Y_S}(\mathcal{M}, \alpha, \beta) &= C_{Y_1}(\mathcal{M}) \sin \beta + C_{Y_3}(\mathcal{M}) \cos \alpha \sin \beta \cos \beta, \\
 C_{Z_S}(\mathcal{M}, \alpha, \beta) &= C_{Z_2}(\mathcal{M}) \sin \alpha \cos \beta, \\
 C_{m_S}(\mathcal{M}, \alpha, \beta) &= C_{m_2}(\mathcal{M}) \sin \alpha \cos \beta + C_{m_4}(\mathcal{M}) \sin \alpha \cos \alpha \cos^2 \beta, \\
 C_{n_S}(\mathcal{M}, \alpha, \beta) &= C_{n_1}(\mathcal{M}) \sin \beta + C_{n_3}(\mathcal{M}) \cos \alpha \sin \beta \cos \beta.
 \end{aligned} \tag{1.31}$$

Model₂: it models the relevance of the mutually independent variation of each incidence angle by means of uncorrelated regression coefficients, corresponding to either α or β coefficient derivatives. Thus, no bilinear terms are included in the model in comparison to Model₁. The order of the selected multivariable polynomial regression models is consistent with (or lower than) the corresponding Model₁ counterparts:

$$\begin{aligned}
 C_{X_S}(\mathcal{M}, \alpha, \beta) &= C_{X_{\alpha 0}}(\mathcal{M}) + C_{X_{\alpha 2}}(\mathcal{M}) \sin^2 \alpha \\
 &\quad + C_{X_{\beta 2}}(\mathcal{M}) \sin^2 \beta + C_{X_{\alpha 4}}(\mathcal{M}) \sin^4 \alpha + C_{X_{\beta 4}}(\mathcal{M}) \sin^4 \beta, \\
 C_{Y_S}(\mathcal{M}, \alpha, \beta) &= C_{Y_{\alpha 1}}(\mathcal{M}) \sin \alpha + C_{Y_{\beta 1}}(\mathcal{M}) \sin \beta, \\
 C_{Z_S}(\mathcal{M}, \alpha, \beta) &= C_{Z_{\alpha 1}}(\mathcal{M}) \sin \alpha + C_{Z_{\beta 1}}(\mathcal{M}) \sin \beta, \\
 C_{m_S}(\mathcal{M}, \alpha, \beta) &= C_{m_{\alpha 1}}(\mathcal{M}) \sin \alpha + C_{m_{\beta 1}}(\mathcal{M}) \sin \beta + C_{m_{\alpha 3}}(\mathcal{M}) \sin^3 \alpha \\
 &\quad + C_{m_{\beta 3}}(\mathcal{M}) \sin^3 \beta + C_{m_{\alpha 5}}(\mathcal{M}) \sin^5 \alpha + C_{m_{\beta 5}}(\mathcal{M}) \sin^5 \beta, \\
 C_{n_S}(\mathcal{M}, \alpha, \beta) &= C_{n_{\alpha 1}}(\mathcal{M}) \sin \alpha + C_{n_{\beta 1}}(\mathcal{M}) \sin \beta.
 \end{aligned} \tag{1.32}$$

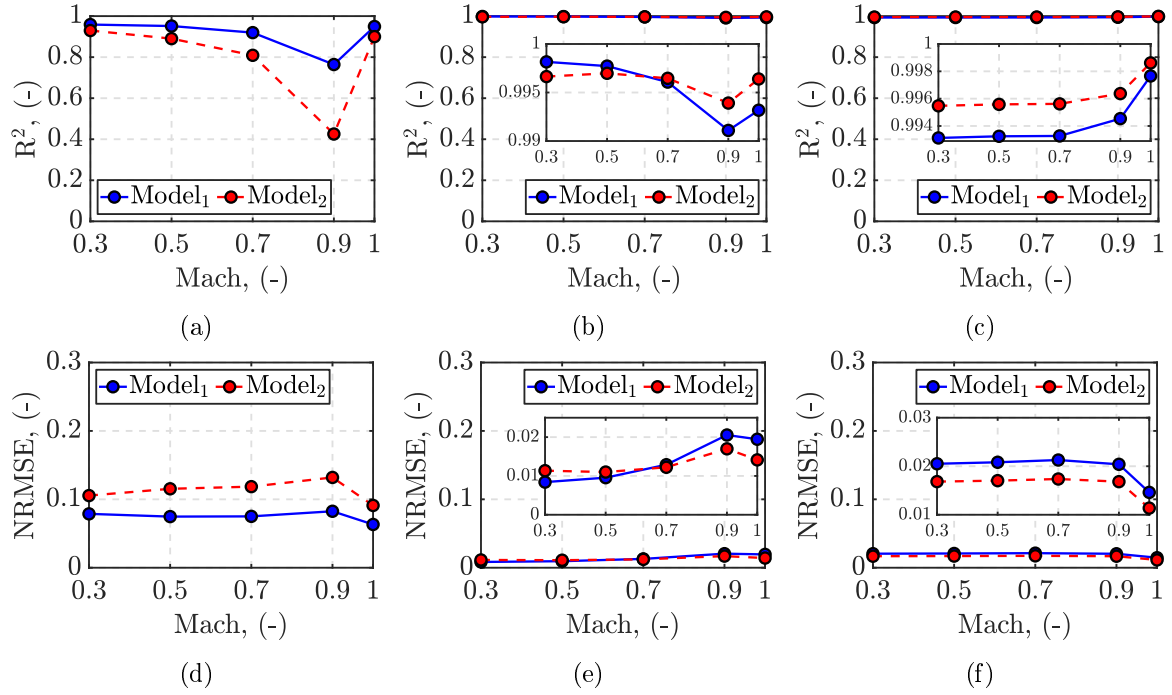


Figure 1.13: R^2 and NRMSE regression results: (a)-(d) longitudinal force coefficient, C_{X_S} ; (b)-(e) lateral force coefficient, C_{Y_S} ; (c)-(f) vertical force coefficient, C_{Z_S} .

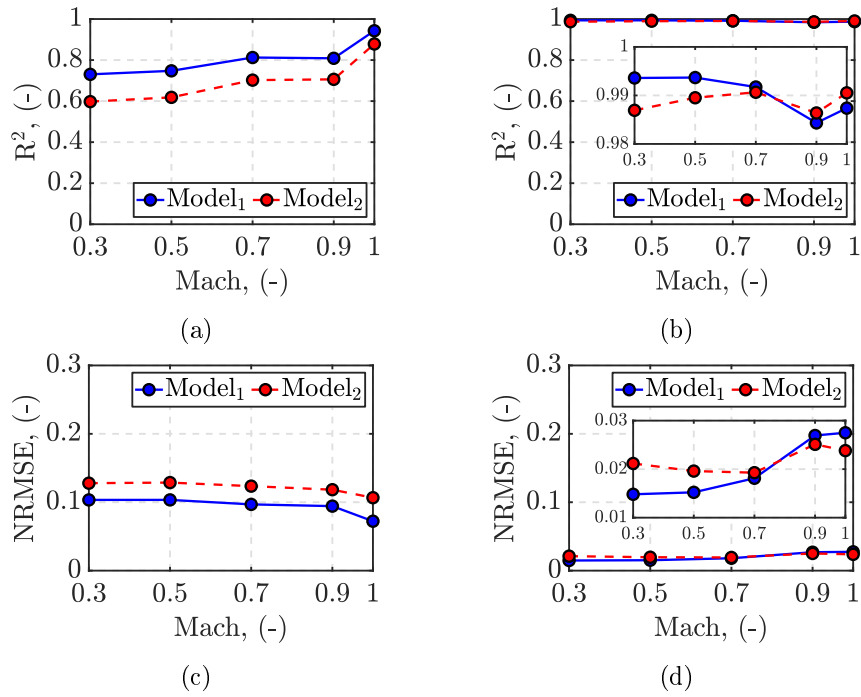


Figure 1.14: R^2 and NRMSE regression results: (a)-(c) pitching moment coefficient, C_{m_S} ; (b)-(d) yawing moment coefficient, C_{n_S} .

As for the *Polynomial Regression*, the accuracy of the investigated models is assessed through the statistical indexes (NRMSE, R^2). The results in Figures 1.13-1.14 show how the Model₁ regression provides a more generally accurate description of the projectile aerodynamics w.r.t. the full CFD dataset. Additionally, in the limit configurations (Conf₁, Conf₂) the Model₁ better approximates the results obtained with the dedicated PR model. In particular, in the Conf₁ scenario ($\beta = 0$) the lateral coefficients (C_{Y_S} , C_{n_S}) should have ideally zero impact on the projectile aerodynamics because of the Dynamic Decoupling Assumption 1.5. Similarly, Conf₂ ($\alpha = 0$) implies ideally zero pitch contributions (C_{Z_S} , C_{m_S}).

These conditions are clearly respected by the multivariable model Model₁, while a parasitic contribution would appear in simulation if the Model₂ model were to be employed. As a consequence the Model₁ in Equation (1.31) is selected and referred to as *Multivariable Regression* model (MR) for the rest of the dissertation. As a general consideration, the pitching moment, C_{m_S} , turned out to be the toughest coefficient to be properly modeled because of the highly nonlinear influence deriving from both the α and the β variations. Once again, the rolling moment coefficient, C_{l_S} , has not been included in the model in reason of the negligible magnitude observed in the acquired data.

1.3.3.3 Regression Approaches Comparison

The previous sections have dealt with the derivation of the aerodynamic regression models (PR and MR) selected to fit the CFD dataset describing the projectile aerodynamics. The *Polynomial Regression* model in Equation (1.30) relies only on a reduced set of the available data, corresponding to the limit configurations, Conf₁ and Conf₂. Despite the lack of accuracy guarantees at more general flight conditions, this model complies with the Decoupling Assumptions 1.5-1.6. Thus, it will be employed at the control design stage for the decoupled channels autopilot. Differently, the *Multivariable Regression* model in Equation (1.31) accounts for all the acquired CFD data, providing a more global description of the projectile aerodynamics across a wider flight envelope. As a consequence, this model is more suitable for simulation purposes and will be implemented in the complete simulator environment.

Since the PR and MR models were derived from different CFD datasets, their accuracy cannot be directly compared at different flight conditions through the statistical results obtained in Section 1.3.3.1 and Section 1.3.3.2. To deal with this issue, a dedicated accuracy analysis has been developed between the two models, targeting the full range of \mathcal{M} , ϕ' , and α' investigated during the CFD campaigns. The value of each aerodynamic coefficient is interpolated first directly on the CFD surfaces as a ground truth reference. Then, the same interpolation is performed on the modeled surfaces obtained through the two regression approaches (PR, MR). The interpolation error corresponds to the RMSE of the difference between the results provided by the CFD coefficient interpolations, $C_{j,CFD}$, and the selected model ones, $C_{j,PR}$ or $C_{j,MR}$, for $j = X, Y, Z, l, m, n$. The RMSE is evaluated along the α' variation by selecting iteratively a specific pair of (\mathcal{M}, ϕ') . These settings allow observing the accuracy of the models as a function of the increasing roll configuration and consequently of the different (α, β) combinations, as well as of \mathcal{M} .

The complete analysis algorithm is presented hereafter.

Algorithm 1 Interpolation Accuracy Analysis

For any $j = X, Y, Z, l, m, n$:

For any $(\mathcal{M}, \phi', \alpha')$ combination:

1. Select the flight condition: $(\mathcal{M}, \phi', \alpha')$.
2. Convert the incidence angles, based on Equation (1.28):

$$(\alpha, \beta) = f(\phi', \alpha').$$

3. Interpolate on the CFD surfaces:

$$C_{j,\text{CFD}} = \text{interp}(\mathcal{M}, \phi', \alpha').$$

3. Interpolate on the PR and MR models:

$$C_{j,\text{PR}} = \text{interp}(\mathcal{M}, \alpha, \beta); \quad C_{j,\text{MR}} = \text{interp}(\mathcal{M}, \alpha, \beta).$$

4. Evaluate the interpolation NRMSE of the PR model as:

$$\text{NRMSE}_{j,\text{PR}}(\mathcal{M}, \phi') = \frac{\text{RMSE}_{j,\text{PR}}(\mathcal{M}, \phi')}{C_{j,\text{CFD},\text{Min-Max}}(\mathcal{M}, \phi')},$$

with

$$\begin{aligned} \text{RMSE}_{j,\text{PR}}(\mathcal{M}, \phi') &= \sqrt{\frac{\sum_{i=1}^n (C_{j,\text{PR}}(\mathcal{M}, \alpha_i, \beta_i) - C_{j,\text{CFD}}(\mathcal{M}, \phi', \alpha'_i))^2}{n}}, \\ C_{j,\text{CFD},\text{Min-Max}}(\mathcal{M}, \phi') &= \max_{\alpha'} (C_{j,\text{CFD}}(\mathcal{M}, \phi', \alpha')) - \min_{\alpha'} (C_{j,\text{CFD}}(\mathcal{M}, \phi', \alpha')), \end{aligned}$$

where n is the dimension of the investigated α' range.

5. Repeat (4.) to evaluate the NRMSE of the MR model.

end.

end.

Samples of the results obtained from the analysis are displayed in Figure 1.15 and Figure 1.16, concerning the interpolation error of the vertical and lateral force coefficients, respectively, as a function of the roll configuration. As expected, at the limit configurations, Conf₁ ($\phi' = 0$ deg) and Conf₂ ($\phi' = 90$ deg), the PR model better approximates the aerodynamics of the projectile, as shown in Figure 1.15(a) (Conf₁) and Figure 1.16(c) (Conf₂). Nevertheless, as soon as the aerodynamic roll is increased, the PR model does not compare any longer with the global MR. Indeed, the effect provided by mutual $\alpha - \beta$ variations is not addressed by the PR model. The complete set of interpolation errors is provided in Appendix A.3.

The results of the analysis confirm the reliability of the two aerodynamic models when

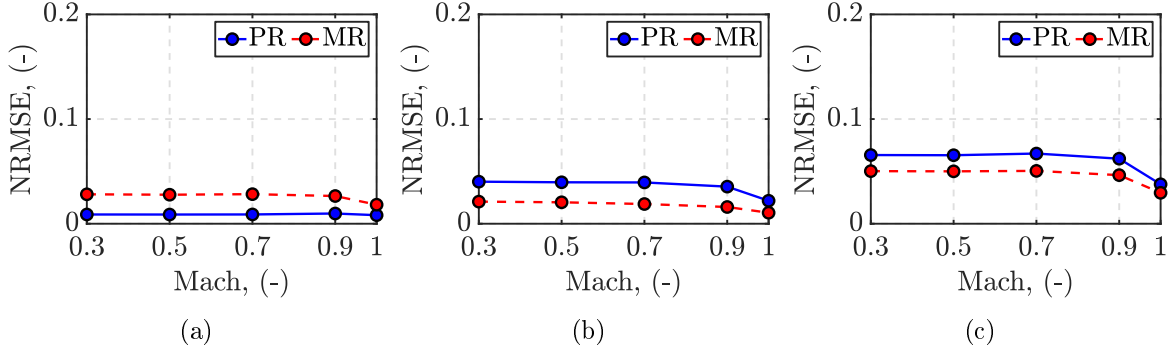


Figure 1.15: C_{Z_s} interpolation NRMSE comparison at different flight conditions: (a) $\phi' = 0$ deg; (b) $\phi' = 30$ deg; (c) $\phi' = 45$ deg.

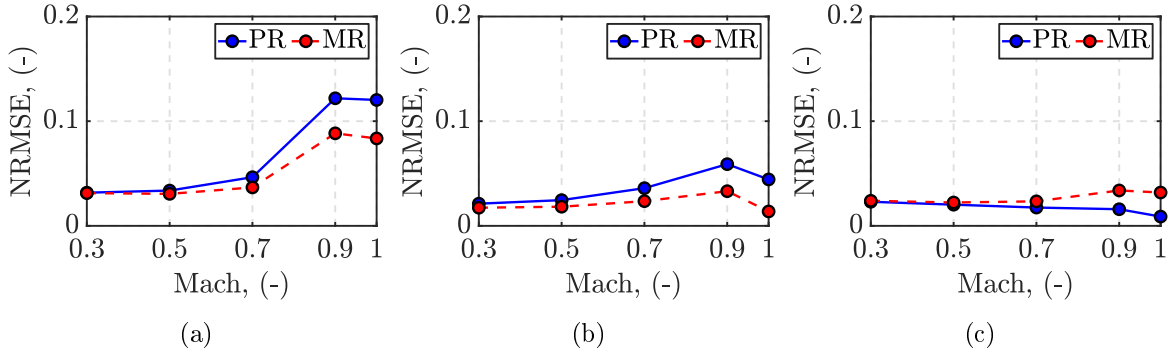


Figure 1.16: C_{Y_s} interpolation NRMSE comparison at different flight conditions: (a) $\phi' = 15$ deg; (b) $\phi' = 45$ deg; (c) $\phi' = 90$ deg.

employed in different configuration scenarios. Even in the worst-case interpolation scenarios for both models, the regression error is always maintained $< 20\%$. In particular, the uncertainties deriving from the limited regression accuracy of PR will be taken into account at the control design stage to ensure the robustness and reliability of the design. Coherently, the uncertainties affecting the MR model, employed in the simulator environment, will serve to test the capability of the controller to handle any source of uncertainties or disturbances.

1.3.3.4 Canards Aerodynamic (Control) Model

The second campaign of CFD simulations discussed in Section 1.3.2.3 was dedicated to the aerodynamic characterization of the right canard local deflection, δ_r . The corresponding left canards coefficients were inferred from the symmetrical properties of the projectile's concept. A polynomial regression approach is employed in the data fitting analysis for the coefficients $C_{X_{\delta_r}}$, $C_{Z_{\delta_r}}$, $C_{l_{\delta_r}}$ and $C_{m_{\delta_r}}$. The same regression model parameterization presented in Equation (1.29) is considered (increasing polynomial orders), accounting for the δ_r variation. The accuracy of the regression analysis is assessed through the standard statistical indexes. The overall results are presented in Figure 1.17 and Figure 1.18, in terms of R^2 and NRMSE.

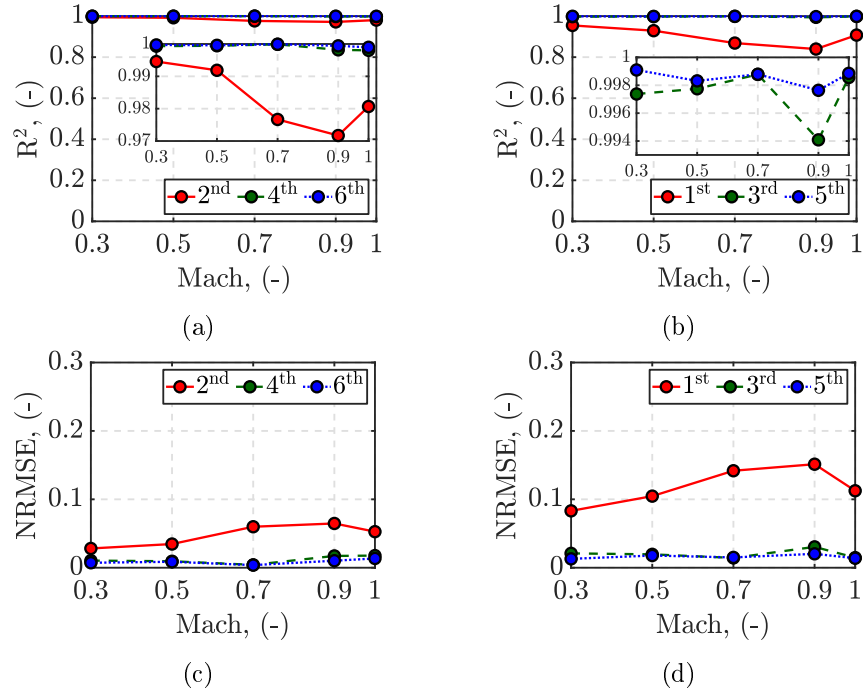


Figure 1.17: R^2 and NRMSE regression results: (a)-(c) longitudinal force control coefficient, $C_{X_{\delta_r}}$; (b)-(d) vertical force control coefficient, $C_{Z_{\delta_r}}$.

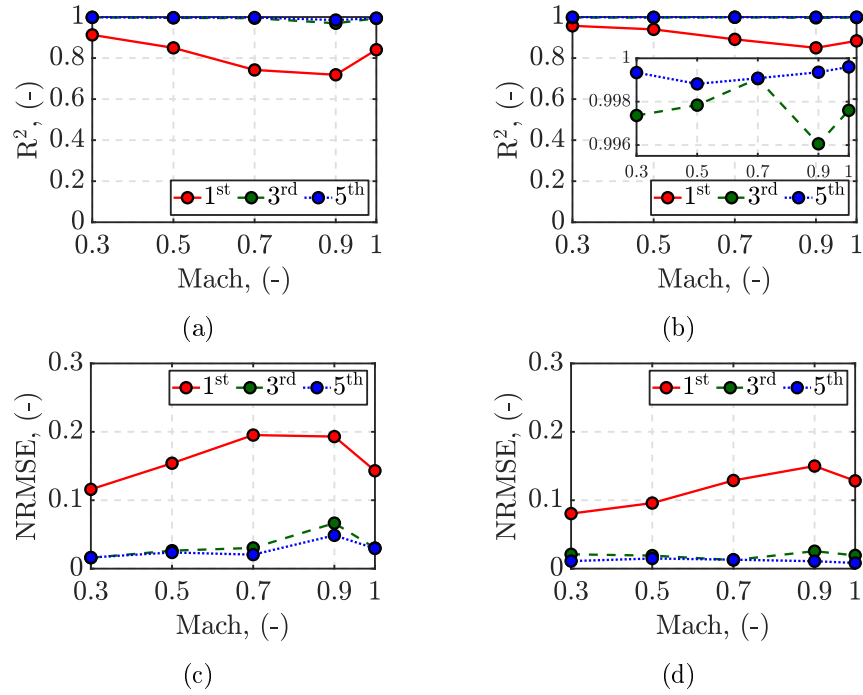


Figure 1.18: R^2 and NRMSE regression results: (a)-(c) rolling moment control coefficient, $C_{l_{\delta_r}}$; (b)-(d) pitching moment control coefficient, $C_{m_{\delta_r}}$.

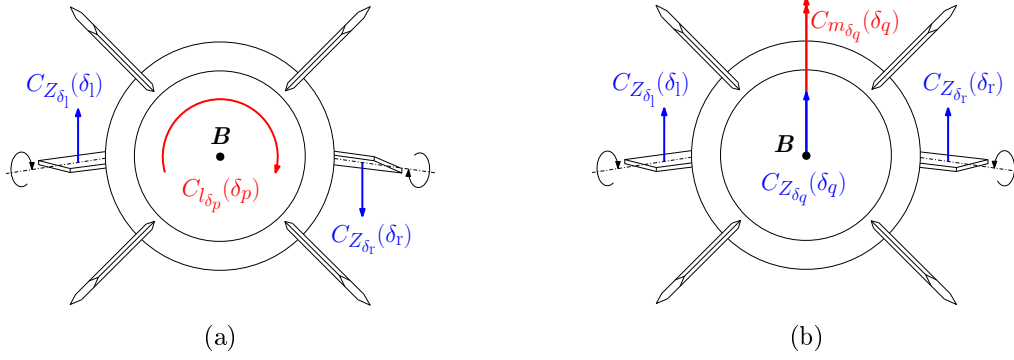


Figure 1.19: Virtual control deflections: (a) roll coefficients; (b) pitch coefficients.

Based on the regression results, the following model is selected to express the right (and left) canard control aerodynamic coefficients:

$$\begin{aligned}
 C_{X_{\delta_r}}(\mathcal{M}, \delta_r) &= C_{X_{\delta_{r0}}}(\mathcal{M}) + C_{X_{\delta_{r2}}}(\mathcal{M}) \sin^2 \delta_r, \\
 C_{Z_{\delta_r}}(\mathcal{M}, \delta_r) &= C_{Z_{\delta_{r1}}}(\mathcal{M}) \sin \delta_r + C_{Z_{\delta_{r3}}}(\mathcal{M}) \sin^3 \delta_r, \\
 C_{l_{\delta_r}}(\mathcal{M}, \delta_r) &= C_{l_{\delta_{r1}}}(\mathcal{M}) \sin \delta_r + C_{l_{\delta_{r3}}}(\mathcal{M}) \sin^3 \delta_r, \\
 C_{m_{\delta_r}}(\mathcal{M}, \delta_r) &= C_{m_{\delta_{r1}}}(\mathcal{M}) \sin \delta_r + C_{m_{\delta_{r3}}}(\mathcal{M}) \sin^3 \delta_r.
 \end{aligned} \tag{1.33}$$

The overall control contributions generated by the canard deflections can be computed by superposition, assuming the aerodynamic response of the canards to be in a linear domain:

$$\begin{aligned}
 C_{X_{\delta}}(\mathcal{M}, \delta) &= C_{X_{\delta_r}}(\mathcal{M}, \delta_r) + C_{X_{\delta_l}}(\mathcal{M}, \delta_l), \\
 C_{Z_{\delta}}(\mathcal{M}, \delta) &= C_{Z_{\delta_r}}(\mathcal{M}, \delta_r) + C_{Z_{\delta_l}}(\mathcal{M}, \delta_l), \\
 C_{l_{\delta}}(\mathcal{M}, \delta) &= C_{l_{\delta_r}}(\mathcal{M}, \delta_r) + C_{l_{\delta_l}}(\mathcal{M}, \delta_l), \\
 C_{m_{\delta}}(\mathcal{M}, \delta) &= C_{m_{\delta_r}}(\mathcal{M}, \delta_r) + C_{m_{\delta_l}}(\mathcal{M}, \delta_l).
 \end{aligned} \tag{1.34}$$

The control allocator in Equation (1.25) converts the individual deflections of the canards into a combined set of virtual contributions, δ_p and δ_q , which is more convenient for control design. Coherently, the aerodynamic model has to address the virtual set of coefficients, $(C_{X_{\delta_{\text{eff}}}}, C_{Z_{\delta_q}}, C_{l_{\delta_p}}, C_{m_{\delta_q}})$ in Figure 1.19, instead of the global contributions in Equation (1.34). Since no CFD measurements of the virtual deflections are available, and according to the superposition hypothesis, the aerodynamic virtual coefficients can be approximated as the direct interpolation of the virtual deflections (δ_p, δ_q) on the available regression surfaces in Equation (1.33). The approximated interpolation is expressed as follows:

$$\begin{aligned}
 C_{Z_{\delta_q}}(\mathcal{M}, \delta_q) &\simeq C_{Z_{\delta_r}}\left(\mathcal{M}, \frac{\delta_r + \delta_l}{2}\right) \simeq \frac{C_{Z_{\delta_r}}(\mathcal{M}, \delta_r) + C_{Z_{\delta_l}}(\mathcal{M}, \delta_l)}{2}, \\
 C_{l_{\delta_p}}(\mathcal{M}, \delta_p) &\simeq C_{l_{\delta_r}}\left(\mathcal{M}, \frac{\delta_l - \delta_r}{2}\right) \simeq \frac{C_{l_{\delta_l}}(\mathcal{M}, \delta_l) - C_{l_{\delta_r}}(\mathcal{M}, \delta_r)}{2}, \\
 C_{m_{\delta_q}}(\mathcal{M}, \delta_q) &\simeq C_{m_{\delta_r}}\left(\mathcal{M}, \frac{\delta_r + \delta_l}{2}\right) \simeq \frac{C_{m_{\delta_r}}(\mathcal{M}, \delta_r) + C_{m_{\delta_l}}(\mathcal{M}, \delta_l)}{2}.
 \end{aligned} \tag{1.35}$$

Concerning the longitudinal control coefficient, the highly nonlinear behavior characterizing the CFD acquisitions in Figure 1.10(a) at lower deflection angles implies the definition of a nonlinear interpolation, based on the roll and pitch contribution, $\delta_{\text{eff}} = \sqrt{\delta_p^2 + \delta_q^2}$:

$$C_{X_{\delta_{\text{eff}}}}(\mathcal{M}, \delta_{\text{eff}}) \simeq C_{X_{\delta_r}}\left(\mathcal{M}, \sqrt{\delta_p^2 + \delta_q^2}\right) \simeq \frac{C_{X_{\delta_r}}(\mathcal{M}, \delta_r) + C_{X_{\delta_l}}(\mathcal{M}, \delta_l)}{2}. \quad (1.36)$$

The approximations accuracy relies on the assumption of a linear aerodynamic response of the canards. To analyze the range of validity of Equations (1.35)-(1.36), an interpolation analysis targets the entire deflection ranges, $\delta_r, \delta_l \in [-36, 36]$ deg, and Mach values investigated during the CFD simulations. The analysis is based on the Algorithm 2, where a linearity error, e_N , is evaluated at each flight condition as the difference between the global coefficients in Equation (1.34), interpolated on the CFD surfaces, and the approximated virtual ones in Equations (1.35)-(1.36), interpolated on the regression models. The results are normalized by the corresponding average value of the CFD surface interpolated at the same Mach conditions.

The results in Figures 1.20-1.23 show the influence of the Mach variation on the linearity error of the coefficients $C_{X_{\delta_{\text{eff}}}}$, $C_{Z_{\delta_q}}$, $C_{l_{\delta_p}}$, $C_{m_{\delta_q}}$, respectively. The error is represented in terms of level contours of increasing values. As expected, the deflection range corresponding to a linearity error $e_l \leq 10\%$ is generally wider at a lower Mach value, $\mathcal{M} < 0.7$, while it tends to increase when approaching the transonic flight regime. The only exception is represented by the longitudinal coefficient in Figure 1.20, which shows low error at any conditions due to the nonlinear nature of the interpolation selected in Equation (1.36). Finally, the order of complexity of the polynomial regression models in Equation (1.33) also affects the accuracy of the interpolation since the regression process is an additional source of model uncertainties. Higher-order models would provide lower interpolation error, but they would explode the complexity at the control design stage.

As a global result, the linear approximations formulated in Equations (1.35)-(1.36) provide reliable modeling properties for canard deflections $|\delta_r|, |\delta_l| < 20$ deg, preventing possible stall conditions characterizing the CFD curves in Figure 1.10.

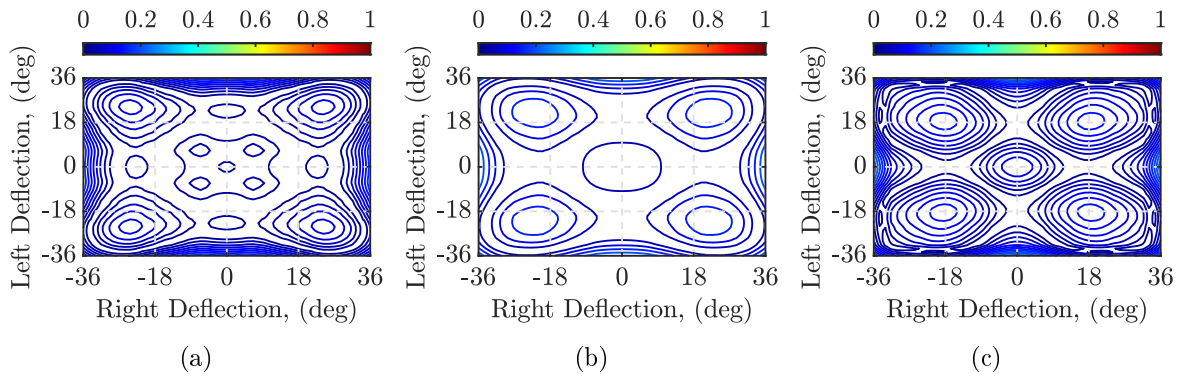


Figure 1.20: $C_{X_{\delta_{\text{eff}}}}$ coefficient linearity error surfaces at different flight regimes: (a) $\mathcal{M} = 0.3$; (b) $\mathcal{M} = 0.7$; (c) $\mathcal{M} = 1$.

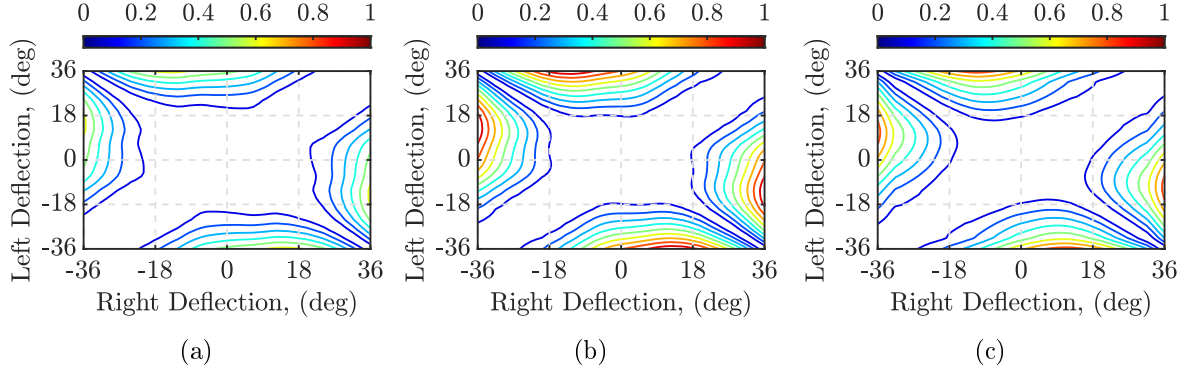


Figure 1.21: $C_{Z_{\delta_q}}$ coefficient linearity error surfaces at different flight regimes: (a) $\mathcal{M} = 0.3$; (b) $\mathcal{M} = 0.7$; (c) $\mathcal{M} = 1$.

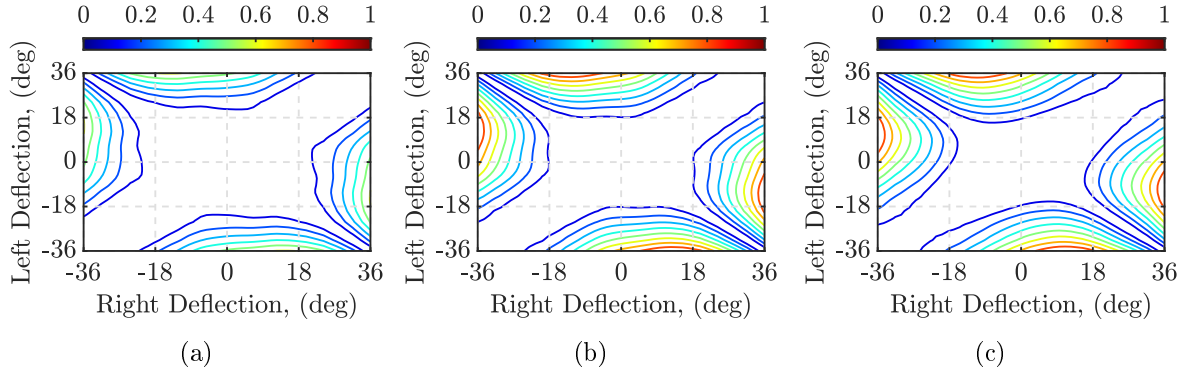


Figure 1.22: $C_{l_{\delta_p}}$ coefficient linearity error surfaces at different flight regimes: (a) $\mathcal{M} = 0.3$; (b) $\mathcal{M} = 0.7$; (c) $\mathcal{M} = 1$.

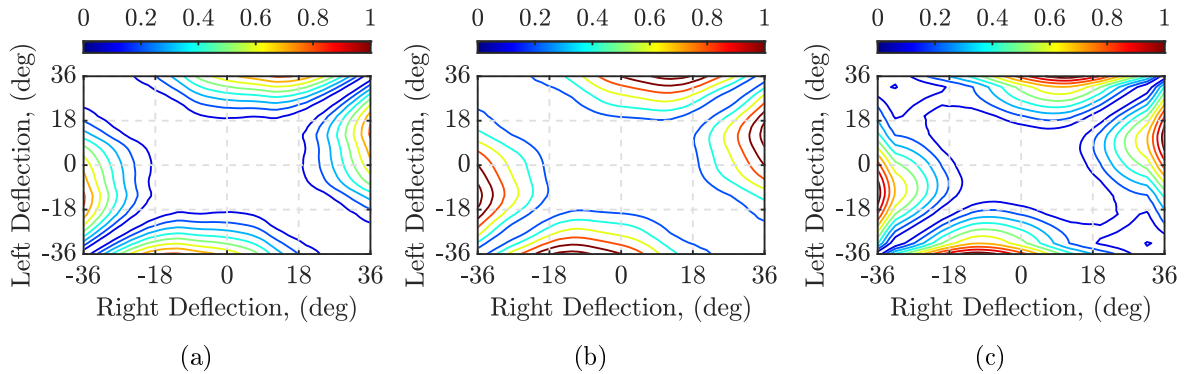


Figure 1.23: $C_{m_{\delta_q}}$ coefficient linearity error surfaces at different flight regimes: (a) $\mathcal{M} = 0.3$; (b) $\mathcal{M} = 0.7$; (c) $\mathcal{M} = 1$.

Algorithm 2 Linearity Error Analysis

For any $j = X, Z, l, m$:

For any \mathcal{M} :

For any (δ_r, δ_l) combination:

1. Select the flight condition: $(\mathcal{M}, \delta_r, \delta_l)$.
2. Convert the deflection angles, based on the allocation logic in Equation (1.25):

$$(\delta_{\text{eff}}, \delta_q, \delta_p) = f(\delta_r, \delta_l).$$

3. Interpolate δ_r and δ_l on the CFD surfaces:

$$C_{j_{\delta_r}, \text{CFD}} = \text{interp}(\mathcal{M}, \delta_r); \quad C_{j_{\delta_l}, \text{CFD}} = \text{interp}(\mathcal{M}, \delta_l),$$

and evaluated the global coefficients as in Equation (1.34):

$$C_{j_{\delta}, \text{CFD}}(\mathcal{M}, \delta_r, \delta_l) = C_{j_{\delta_l}, \text{CFD}} + C_{j_{\delta_r}, \text{CFD}}; \quad \text{if } j = X, Z, m.$$

$$C_{j_{\delta}, \text{CFD}}(\mathcal{M}, \delta_r, \delta_l) = C_{j_{\delta_l}, \text{CFD}} - C_{j_{\delta_r}, \text{CFD}}; \quad \text{if } j = l.$$

4. Interpolate δ_{eff} , δ_q or δ_p on the regression models in Equation (1.33):

$$C_{j_{\delta_{\text{eff}}}} = \text{interp}(\mathcal{M}, \delta_{\text{eff}}); \quad \text{if } j = X.$$

$$C_{j_{\delta_q}} = \text{interp}(\mathcal{M}, \delta_q); \quad \text{if } j = Z, m.$$

$$C_{j_{\delta_p}} = \text{interp}(\mathcal{M}, \delta_p); \quad \text{if } j = l.$$

5. Evaluate the normalized linearity error as:

$$e_{j,N}(\mathcal{M}, \delta_r, \delta_l) = \frac{e_j(\mathcal{M}, \delta_r, \delta_l)}{\bar{C}_{j, \text{CFD}}(\mathcal{M})},$$

with

$$e_j(\mathcal{M}, \delta_r, \delta_l) = C_{j_{\delta_h}}(\mathcal{M}, \delta_i) - C_{j_{\delta}, \text{CFD}}(\mathcal{M}, \delta_r, \delta_l); \quad \text{for } h = \text{eff}, q, p.$$

$$\bar{C}_{j, \text{CFD}}(\mathcal{M}) = \frac{\sum_{i=1}^n \sum_{k=1}^n C_{j, \text{CFD}}(\mathcal{M}, \delta_{r,i}, \delta_{l,k})}{n^2},$$

 where n is the dimension of the investigated δ_r , δ_l range.

end.
end.
end.

1.4 6-DoF Simulator Environment

The results obtained in the previous sections are implemented in a complete nonlinear flight simulator environment, meant to be later employed in the validation phase of the autopilot design. The simulator is designed in the MATLAB/Simulink environment, by means of the dedicated System Modeling Ammunition Research Toolbox (SMART) library developed at ISL and presented in Section 1.4.1. The complete architecture of the simulator is discussed in Section 1.4.2, while ballistic simulations are employed in Section 1.4.3 to validate the overall environment design.

1.4.1 The SMART Toolbox

The System Modeling Ammunition Research Toolbox (SMART) Simulink library consists of a project proposed and developed in the past fifteen years at the French-German Research Institute of Saint-Louis. The core idea was to provide a standardized and common software environment to perform the guidance, navigation, and control design of several models of aircraft, missiles, and projectiles. The first version of the environment was initially coded in FORTRAN and consisted of an exterior ballistic 6-DoF simulator, which did not include any control design features. Later in 2004, the Computer Aided Design of Aerospace Concepts (CADAC) presented in [Zip14] was employed as a reference model for the development of the Simulink environment, extending the modeling features to the rolling and the non-spinning dynamic frames of the vehicle's airframe ([Wer07]). In 2013 a complete version of the simulation environment allowed selecting among several projectile/missile dynamic models and integrating guidance, navigation, and control features in the same simulation. The library consists of generalized Simulink blocks whose parameters can be tuned to implement both vehicle dynamics and atmosphere models, as well as different control architectures, guidance strategies, and navigation algorithms ([GWT13]). The library finally addressed as SMART, has been further developed in the last few years by including spinning projectile models.

1.4.2 Nonlinear Simulator

The nonlinear simulator intends to provide an accurate representation of the flight conditions in which the controller is supposed to operate. Thus, it targets the flight dynamics of the projectile, as well as the dynamics of the environment including the atmosphere properties, unwanted wind disturbances, and the gravitational effect. The scheme in Figure 1.24 exhibits the complete architecture of the simulation environment developed in Simulink, addressing each aspect of the standard GNC loop.

Guidance. The guidance Simulink block allows implementing different flight strategies depending on the objectives that are selected for a specific simulation. As introduced in Section 1.2.4, the LRGP project aims to improve the operating range of standard guided ammunition.

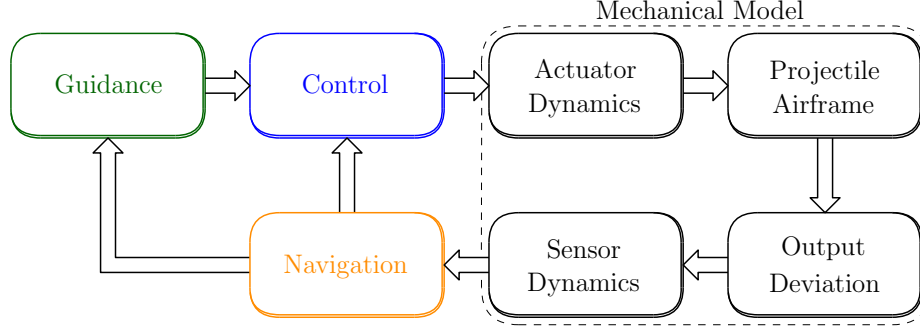


Figure 1.24: Nonlinear simulator: complete software environment.

Coherently with the purposes of the project, the guidance block implements online the LDR optimization law proposed in [KCL82]. The algorithm provides a trade-off between highly complicated head-on approaches and sub-optimal architectures based on a set of open-loop offline evaluations of a standard pitch-attitude dynamics. Assuming quasi-steady state glide equilibrium conditions with approximately constant dynamic pressure for the 2-DoF pitch-attitude dynamics, and assuming that an optimal Lift-to-Drag Ratio, LDR_{\max} , exists at each flight condition, the corresponding equilibrium flight-path angle, γ_{eq} , can be expressed as:

$$\gamma_{\text{eq}} = -\frac{1}{\text{LDR}_{\max} |1 + \beta_{\text{atm}} (\frac{V^2}{2g})|} \quad (1.37)$$

where $\beta_{\text{atm}} = 1.389 \cdot 10^{-4} \text{ 1/m}$ represents the exponent of the atmosphere density, modeled as $\rho_{\text{atm}} = \rho_{\text{atm},0} e^{-\beta_{\text{atm}} h}$ with $\rho_{\text{atm},0} = 1.227 \text{ kg/m}^3$. A reference AoA command, α_{ref} , can be derived from the combination:

$$\alpha_{\text{ref}} = \alpha_{\text{LDR},\max} + k_{\gamma} (\gamma_{\text{eq}} - \gamma) \quad (1.38)$$

where $\alpha_{\text{LDR},\max}$ consists of the optimal AoA, obtained by trimming the pitch-attitude dynamics at each LDR_{\max} condition, and γ is the actual flight-path angle measured along the trajectory. The coefficient k_{γ} allows adjusting the relevance of the flight-path angle correction with respect to the trimmed $\alpha_{\text{LDR},\max}$, aiming to find an optimal trade-off and to avoid excessively sharp variations of the resulting reference signal. For the present study, $k_{\gamma} = 0.35$ has been selected, and a dataset of $(\text{LDR}_{\max}, \alpha_{\text{LDR},\max})$ has been provided through dedicated CFD campaigns on the complete projectile dynamics to increase the accuracy.

Navigation. The navigation block allows the implementation of any kind of estimation algorithm or measurement processing to determine the current state of the system. During the controller design, perfect navigation conditions (accurate and undelayed) are assumed. However, at the validation stage, sensor noise (measurement noise) should be taken into account for a more realistic simulation scenario.

Control. The control block includes the designed autopilot to be tested in simulation. This represents the core objective of the present work, and it will be treated in detail in Chapter 3

and Chapter 4, where different LPV-based controller design approaches and architectures will be proposed and eventually compared.

Actuator and Sensor Dynamics. The impact of the actuators and the sensor dynamics is also accounted for, aiming to improve the accuracy of the simulator. In particular, the actuators are modeled as second-order systems characterized by the following transfer function:

$$T_{\text{act}} = \frac{\omega_{\delta}}{s^2 + 2\omega_{\delta}\xi_{\delta}s + \omega_{\delta}^2} \quad (1.39)$$

where $\omega_{\delta} = 150$ rad/s is the actuator bandwidth, and $\xi_{\delta} = 0.707$ represents the damping ratio. Additionally, angular position and angular rate saturation are also addressed, respectively as the ranges $[-40, 40]$ deg, and $[-100, 100]$ deg/s.

Projectile Airframe. The airframe block contains a complete description of the flight mechanics, the environment, and the generation of the aerodynamic contributions, as presented in Figure 1.25. In particular, the *Environment Model* provides a general representation of the atmosphere following the International Standard Atmosphere (ISA) 1975, ISO 2533 ([Atm]). In addition, it includes continuous and discrete models of the wind contributions (turbulence, gusts), employed as sources of disturbance to assess the robustness of the controller in more realistic scenarios. Further details will be provided in Chapter 4.

Concerning the *Aerodynamic Model*, the *Multivariable Regression* static model (Model₁ in Equation (1.31)), and the control contributions described in Equations (1.33)-(1.36) are employed in the simulator environment. Based on a significant CFD dataset, this model allows accounting for all the possible flight configurations that the projectile might experience during the trajectory. The *Flight Mechanics* block implements the 6-DoF model of the projectile, including the dynamic and kinematic equations of motion discussed in Equations (1.12)-(1.13), and Equations (1.14)-(1.17) respectively. Finally, the control allocator converts the individual right and left canards' deflections into combined pitch and roll contributions, as previously expressed in Equation (1.25).

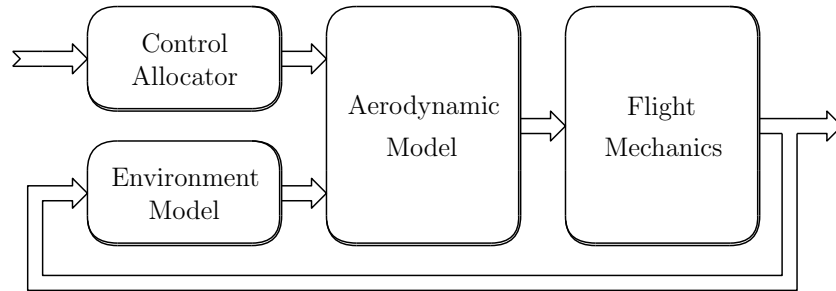


Figure 1.25: Nonlinear simulator: projectile airframe architecture.

1.4.3 Model Validating Simulations

The validation of the nonlinear simulator environment relies on open-loop ballistic simulations, targeting each phase of the projectile trajectory:

- I. Ballistic ascending phase (from the firing point to the apogee).
- II. Ballistic gliding phase (from the apogee to the target).

In particular, during phase I, the projectile is in the ballistic configuration shown in Figure 1.4(b), having the control surfaces folded inside the sabot. Thus, the projectile aerodynamics is based on the online interpolation of the static coefficient surfaces acquired through the first CFD campaign. The firing stage consists of an initial elevation angle $\theta_e = 60$ deg at zone 6, equivalent to an initial longitudinal velocity of approximately $u_0 = 939$ m/s. The projectile is supposed to be ideally fired with almost no spin, in reason of the fin-stabilized architecture. Any residual spinning motion is expected to be damped during the ascending phase by the opposing Drag generated by the fins.

Concerning the ballistic gliding phase II, Figure 1.26 highlights the comparison between a gliding phase characterized by a ballistic configuration where the canards are not deployed at the apogee of the trajectory (dashed blue), and a gliding phase assuming a glider configuration in Figure 1.4(b) with the canards fully deployed and maintained at zero local deflection angles, $\delta_r, \delta_l = 0$ deg (solid red). The former trajectory depends on the aerodynamic CFD dataset interpolation employed for the ballistic ascending phase. Differently, the glider-based trajectory relies on the *Multivariable Regression* model described in the *Projectile Airframe* paragraph. Since no guidance references are provided and zero control actions are applied on the projectile across the trajectory, the terminal guidance phase is not considered for the simulation. Similarly, the lateral dynamics of the projectile is also neglected due to the absence of lateral steering maneuvers and wind contributions.

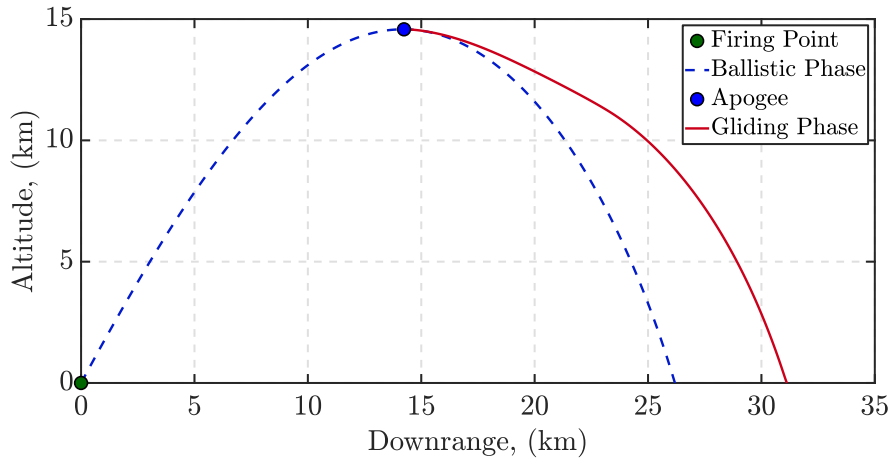


Figure 1.26: Ballistic simulations: trajectory performance comparison.

The trajectory results in Figure 1.26 show the range enhancement provided by the additional lifting contribution of the control surfaces, even in the absence of direct control commands. However, the canard contributions generate a relevant destabilizing effect on the projectile aerodynamics, since the overall CP, where the aerodynamic forces are ideally applied, is pushed ahead of the projectile CM. This destabilizing effect is consistent with the CFD data acquired during the aerodynamic characterization of the projectile, and it is highlighted by the oscillation affecting the results in Figures 1.27(a)(c)(d)(e).

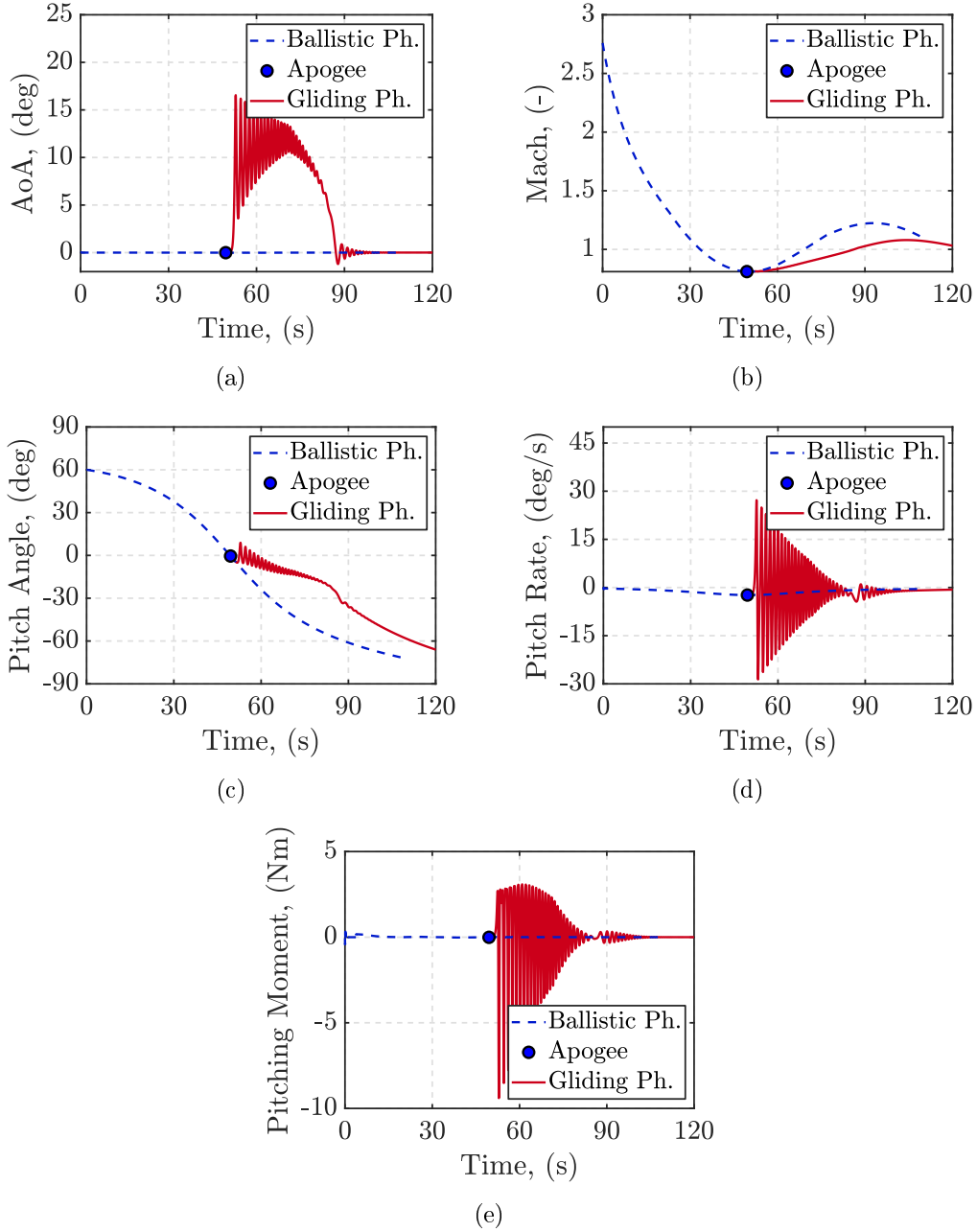


Figure 1.27: Ballistic simulations: (a) AoA trajectories; (b) Mach trajectories; (c) pitch angle trajectories; (d) pitch rate trajectories; (e) pitching moment trajectories.